

RESEARCH

Open Access

# Improving reliability of non-volatile memory technologies through circuit level techniques and error control coding

Chengen Yang<sup>\*</sup>, Yunus Emre, Yu Cao and Chaitali Chakrabarti

## Abstract

Non-volatile resistive memories, such as phase-change RAM (PRAM) and spin transfer torque RAM (STT-RAM), have emerged as promising candidates because of their fast read access, high storage density, and very low standby power. Unfortunately, in scaled technologies, high storage density comes at a price of lower reliability. In this article, we first study in detail the causes of errors for PRAM and STT-RAM. We see that while for multi-level cell (MLC) PRAM, the errors are due to resistance drift, in STT-RAM they are due to process variations and variations in the device geometry. We develop error models to capture these effects and propose techniques based on tuning of circuit level parameters to mitigate some of these errors. Unfortunately for reliable memory operation, only circuit-level techniques are not sufficient and so we propose error control coding (ECC) techniques that can be used on top of circuit-level techniques. We show that for STT-RAM, a combination of voltage boosting and write pulse width adjustment at the circuit-level followed by a BCH-based ECC scheme can reduce the block failure rate (BFR) to  $10^{-8}$ . For MLC-PRAM, a combination of threshold resistance tuning and BCH-based product code ECC scheme can achieve the same target BFR of  $10^{-8}$ . The product code scheme is flexible; it allows migration to a stronger code to guarantee the same target BFR when the raw bit error rate increases with increase in the number of programming cycles.

**Keywords:** MLC PRAM, STT-RAM, Circuit level techniques, Error control coding, Block failure rate

## Introduction

Over the last decade, there has been a significant research effort on designing different types of memory devices that have high data storage density and low leakage power. Many of these works focus on finding an alternative to commonly used SRAM, DRAM, and Flash memories [1,2]. The two most attractive memory technologies that have emerged are phase-change RAM (PRAM) [3,4] and spin transfer torque RAM (STT-RAM) [5-7]. STT-RAM is an attractive candidate for lower level caches because of its fast read and write operation, very low standby power, and high endurance. PRAM, on the other hand, is a promising candidate for high-level cache and external storage due to high density and very low standby power. While single level cell (SLC) PRAM and STT-RAM have comparable memory

densities, multi-level cell (MLC) PRAM has been introduced to improve the memory density even further [8,9]. Unfortunately, MLC-type memories have reliability issues that need to be addressed.

The two competing memory technologies operate in very different ways. While in PRAM, data are stored as a resistance value set by thermal constraints, whereas in STT-RAM it is set by the magnetization angle. The PRAM cell changes between amorphous phase (low resistance) and crystalline phase (high resistance); the value that is stored in the cell is a function of this resistance. The resistance in STT-RAM is a function of the magnetization angle of the magnetic tunneling junction (MTJ). The value that is stored in the cell is based on whether the direction of the magnetization angle is parallel (P) (bit '0') or antiparallel (AP) (bit '1').

As the technology of these emerging memory devices become more mature and they get ready to be adopted in mainstream computers, a study of their reliability

\* Correspondence: chengen.yang@asu.edu  
School of Electrical, Computer and Energy Engineering, Arizona State University, Tempe, AZ 85287, USA

becomes very important. The causes of errors of these two technologies and the techniques that can be used to mitigate them are quite different. For instance, MLC PRAM which has very high storage density has higher error rate because of reduced difference between consecutive resistance levels. The resistance of an intermediate state drifts to that of a state with higher resistance causing soft errors; these errors increase with data storage time [10]. Again the resistance of the amorphous state decreases with the number of programming cycles and causes hard errors. Resistance drift has been studied and a technique to tune the threshold resistance between adjacent states to handle soft errors has been proposed in [11,12]. We analyze the effect of threshold resistance on the total error rate (combination of hard and soft error rates) and show that there is an optimal threshold value for a given data storage time and number of programming cycles. This threshold value can be adjusted using circuit-level techniques to reduce bit error rate (BER) to  $10^{-4}$ .

The source of errors in STT-RAM is quite different from that of PRAM [13-15]. Majority of the errors are due to process variations [13,15]. These include variation of the access transistor sizes ( $W/L$ ), variation in  $V_{th}$  due to random dopant fluctuation (RDF), MTJ geometric variation and thermal fluctuations that are modeled using change in initial magnetization angle of the MTJ [15]. BER due to these variations can be as high as  $10^{-1}$  for write-1 operation [14]. Fortunately, the error rate can be dropped to  $10^{-5}$  by circuit-level techniques such as adjusting  $W/L$  ratio of the access transistor, changing the current pulse width during write, and increasing the voltage across the STT-RAM cell.

Apart from the purely circuit-level techniques, hybrid techniques that consist of circuit techniques followed by error control coding (ECC) have also been proposed to increase the reliability of both PRAM and STT-RAM. For instance for MLC PRAM, Xu and Zhang [11] proposed a hybrid technique that first reduced the soft error rate by adjusting the threshold resistance and then used BCH or LDPC codes on large code words to improve the reliability with high storage efficiency. Since this technique is for mass storage devices, the large latency is not a concern. Another hybrid technique for MLC PRAM has been proposed in [16] where architecture-level techniques such as subblock flipping and bit interleaving followed by BCH( $t = 3$ ) codes have been applied on top of threshold resistance tuning. For STT-RAM, Sun et al. [12] proposed a combination of write-read-verify strategy and Hamming codes to protect against write errors in cache. While the write-read-verify strategy increases the latency and energy, it reduces the error rate significantly and as a result it is sufficient to use simple ECC such as Hamming codes.

In this article, we first study the causes of errors in MLC PRAM and STT-RAM starting from first principles and model the probability of hard and soft errors. In each case, we show how circuit-level techniques can reduce some of the errors. Next, we show how traditional ECC techniques can be used in conjunction with the circuit techniques to further improve the error rate. For instance, for STT-RAM, a combination of circuit parameter tuning and BCH code-based ECC can help achieve block failure rate (BFR) of  $10^{-8}$ . For PRAM, a combination of threshold resistance tuning and BCH-based product code scheme can achieve the same target

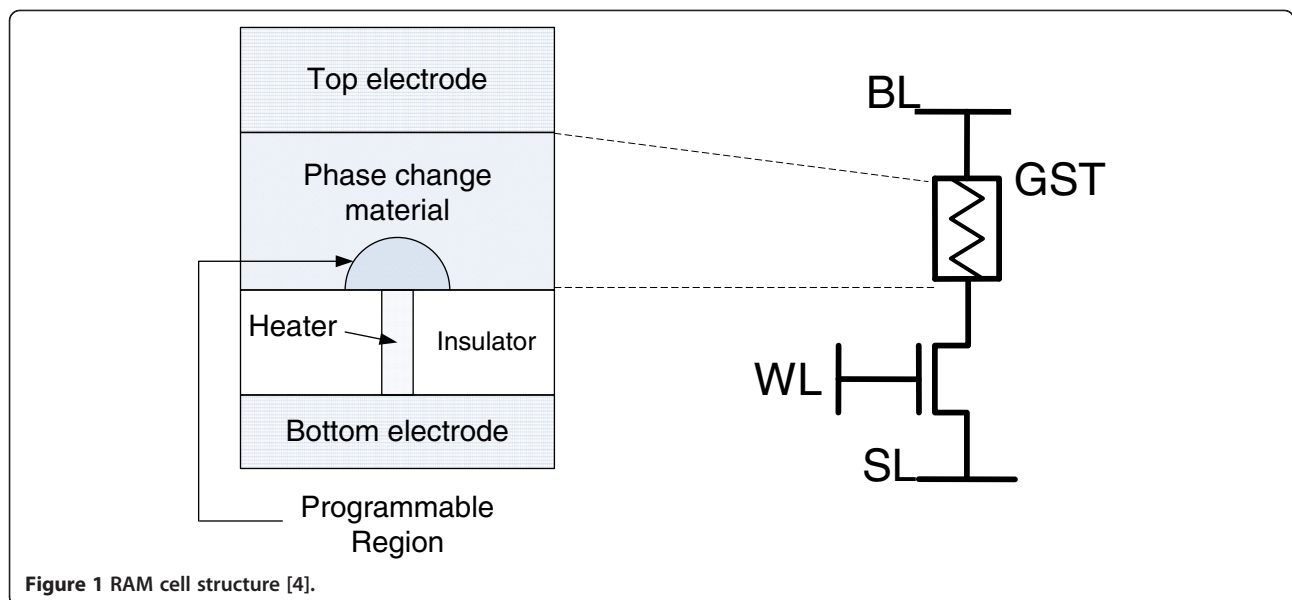
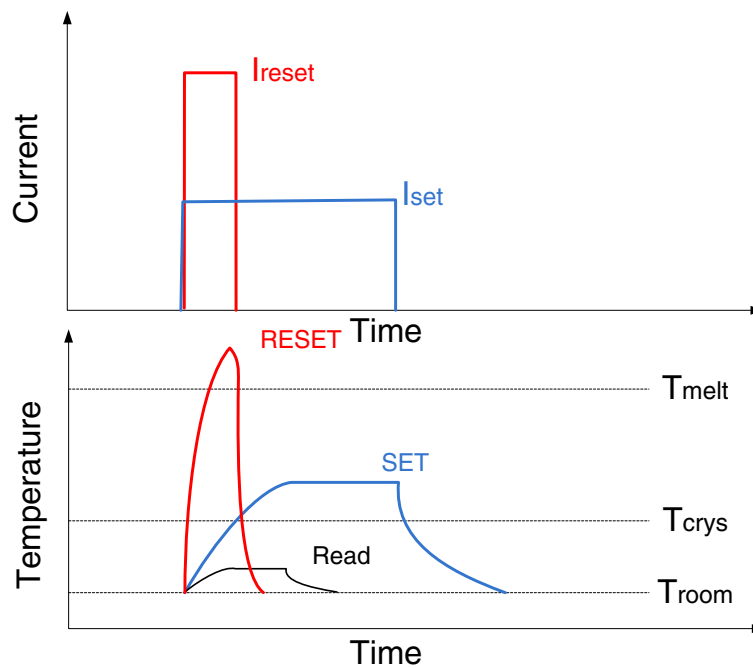


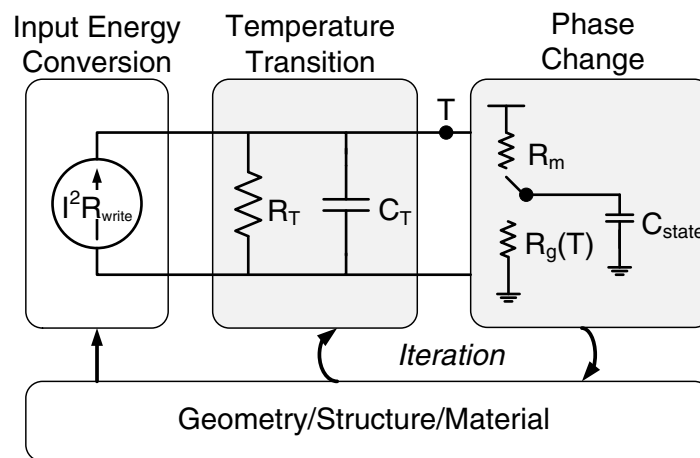
Figure 1 RAM cell structure [4].

BFR. In addition, the proposed product code scheme has the capability to migrate to a stronger ECC when the error rate increases with increase in the number of programming cycles. This study is an extension of [16,17]. The specific contributions of this article are as follows.

- A detailed analysis of errors in MLC PRAM due to resistance drift as a function of data-storage time and number of programming cycles.
- Determination of optimal resistance threshold value that minimizes the overall error rate (hard and soft) for MLC PRAM.
- A detailed study of process variation induced failures in STT-RAM.
- Development of circuit-level techniques for STT-RAM that reduces the error rate due to judicious use of increase in  $W/L$  ratio of the access transistor, higher voltage difference across the



(a)



(b)

**Figure 2** PRAM R/W operations and simulation model. (a) PRAM cells are programmed and read by applying electrical pulses with different characteristics. (b) HSPICE simulation model for programming process [16].

memory cell, and pulse width adjustment in write operation.

- Development of ECC techniques for both MLC-PRAM and STT-RAM that can be used in conjunction with circuit-level techniques to further enhance the reliability. Evaluation of the hardware overhead and error correction performance of the different techniques.

The rest of the article is organized as follows. “PRAM reliability” section describes the sources of soft and hard errors for 2-bit MLC PRAM and proposes circuit-level techniques to reduce them. “STT-RAM reliability” section describes the causes of failures in STT-RAM and proposes circuit parameter tuning to address them. “ECC schemes” section focuses on the details of the ECC schemes for PRAM and STT-RAM with hardware overhead. Finally, the article concludes with some conclusions.

### PRAM reliability

In this section, we describe the basic structure of the PRAM cell including read and write operations (see “Background” section), characterization of its soft errors and hard errors (see “PRAM error model” section), and a circuit-level technique to reduce these errors (see “Circuit-level techniques for reducing soft and hard errors” section).

### Background

Unlike conventional SRAM and DRAM technologies that use electrical charge to store data, in PRAM, the logical value of data corresponds to the resistance of the chalcogenide-based material in the memory cell. Chalcogenide-based material is one of the phase-change materials which can switch between a crystalline phase (low resistance) and an amorphous phase (high resistance) with the application of heat. In PRAM,  $\text{Ge}_2\text{Sb}_2\text{Te}_5$  (GST) is usually used as the phase-change material.

The structure of a PRAM cell is shown in Figure 1. GST is put between the top electrode and a metal heater which is connected to the bottom electrode. The top electrode is connected to bit line (BL) and the bottom electrode is connected to the drain of current driver transistor indicated by select line (SL) node. The current driver transistor is controlled by word line (WL). When voltage is applied between top and bottom electrodes, the current through the heater heats the GST material and changes its phase; the change happens within a certain volume, referred to as the programmable region. The shape of the programmable region is usually considered to be mushroom shape due to the current crowding effect at the heater to phase-change material contact [4].

### SLC PRAM

An SLC PRAM consists of two states, namely SET state corresponding to the low resistance crystalline phase or state “1”, and RESET state corresponding to the high resistance amorphous phase or state “0”. As shown in Figure 2a, in order to change the phase of a PRAM cell from one state to the other, there are two basic write operations: the SET operation that switches the GST into the crystalline phase and the RESET operation that switches the GST into the amorphous phase. For RESET operation, a large current is passed through top and bottom electrodes which heats the programmable region over its melting point. This is followed by a rapid quench which turns this region into an amorphous state. For SET, a lower current pulse is applied for a longer period of time

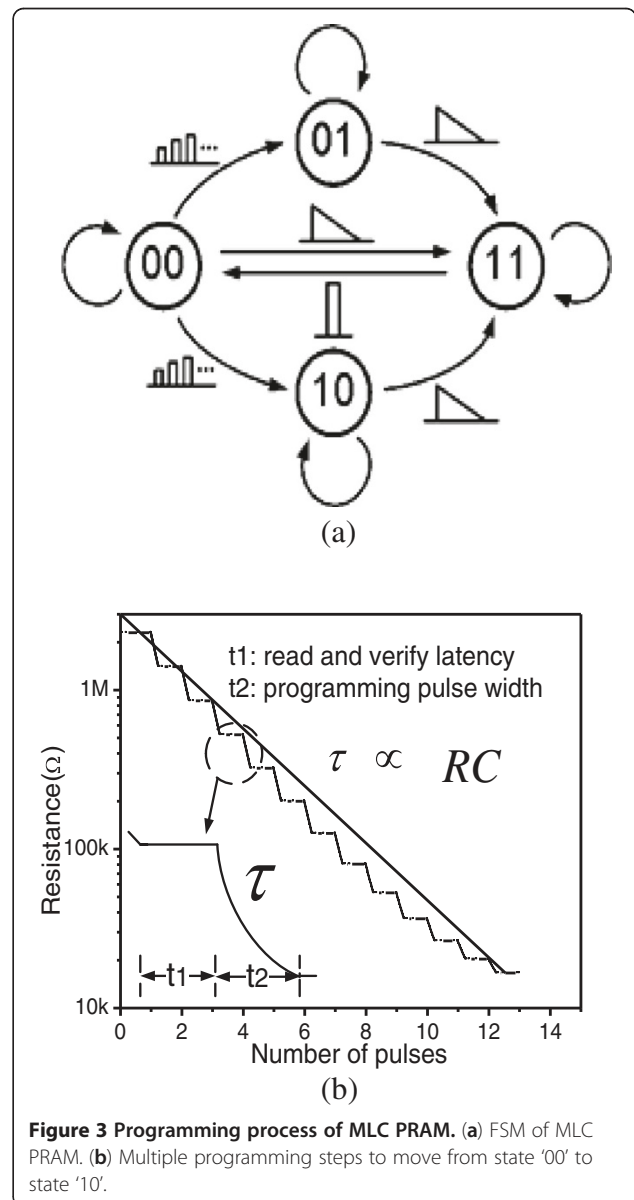


**Figure 3 Programming process of MLC PRAM. (a)** FSM of MLC PRAM. **(b)** Multiple programming steps to move from state ‘00’ to state ‘10’.

**Table 1 Simulation parameters of a 2-bit MLC PRAM**

Parameter	2-bit MLC PRAM				CMOS current driver		
	$R_{00}$	$R_{01}$	$R_{10}$	$R_{11}$	$V_{dd}$	Width	Length
Value	2.3 M $\Omega$	46 k $\Omega$	15 k $\Omega$	10 k $\Omega$	1 V	75 nm	45 nm

so that the programmable region is at a temperature that is slightly higher than the crystallization transition temperature. For READ, a low voltage is applied between the top and bottom electrodes to sense the device resistance. The read voltage is set to be sufficiently high to provide a current that can be sensed by a sense amplifier but low enough to avoid write disturbance [4].

To simulate the programming process of a PRAM cell, an HSPICE model has been developed as shown in Figure 2b. According to this model [18], the equivalent circuit of PRAM consists of four parts: input energy conversion, temperature transition, phase change, and geometry. Here  $R_T$  and  $C_T$  represent the thermal resistance and capacitance of GST structure,  $R_{write}$  is the electrical resistance of GST during programming,  $R_m$  and  $R_{g(T)}$  represent the phase of GST material, and  $C_{state}$  represents the state of the MLC cell. The geometry block describes the cross-sectional shape (mushroom) of the PRAM cell, the dimensions of which are used to calculate the electrical and thermal parameters. The input energy changes the temperature of GST material based on  $R_T$  and  $C_T$ . The temperature evaluated by the temperature transition block is used to decide on the switch position; when the temperature is higher than the melting temperature, the switch flips up and  $C_{state}$  is charged by the voltage source, indicating the melting of GST, which results in the amorphous phase. When the temperature is between the melting and annealing temperature, the switch flips down and  $C_{state}$  is discharged through  $R_g$ , indicating the annealing of GST, which results in the crystalline phase.

**MLC PRAM**

To increase the storage density of memory, MLC is used to store more than 1 bit within a single memory cell

[8,9]. Since the resistance between the amorphous and crystalline phases can exceed two to three orders of magnitude [3], multiple logical states corresponding to different resistance values can easily be accommodated. To study the programming process of MLC PRAM, the simulation model of SLC PRAM in Figure 2b can still be utilized. Note that while for SLC PRAM, the switch between  $R_m$  and  $R_{g(T)}$  can only be set to “ $R_m$ ” or “ $R_{g(T)}$ ” corresponding to amorphous or crystalline phase, for MLC PRAM, the switch is set to an intermediate position between the two ends.

A 2-bit MLC PRAM consist of four states, where ‘00’ is full amorphous state, ‘11’ is full crystalline state, ‘01’ and ‘10’ are two intermediate states. The corresponding finite state machine (FSM) for modeling the WRITE strategy of a 2-bit MLC is shown in Figure 3a [19]. To go to ‘11’ state, a ramp down SET pulse is applied. To go to ‘00’ state from a ‘01’ or ‘10’ state, it first transitions to ‘11’ state to avoid over programming, and then to ‘00’ state. To write ‘01’ or ‘10’, it first transitions to ‘00’ state and then to the final state using several sequential short pulses. Figure 3b shows the resistance values corresponding to multiple programming steps that are required to go from ‘00’ state to ‘10’ state. The method is based on read and verify. During  $t_1$ , the resistance value in the memory cell is read out and compared with the resistance of the final state; if it is higher than the final state resistance, another current pulse of duration  $t_2$  is applied to further lower the resistance. In this article, the static parameters used in the simulation of 2-bit MLC PRAM are listed in Table 1.

**PRAM error model**

**Sources of soft and hard errors**

The reliability of a PRAM cell can be analyzed with respect to data retention, cycling endurance, and data disturb [20]. Data retention represents the capability of storing data reliably over a time period and data retention time is the longest time that the data can be stored reliably. We define ‘storage time’ as the time that the

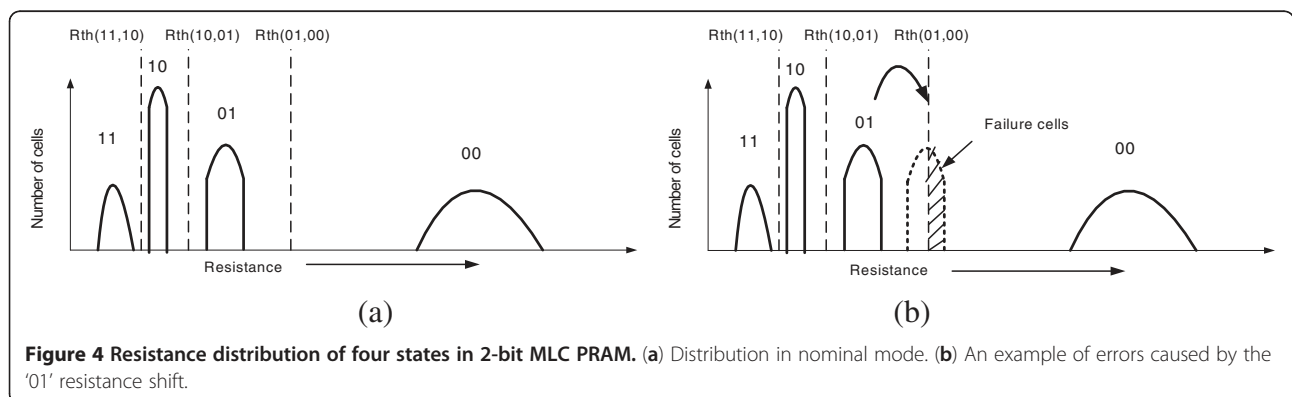
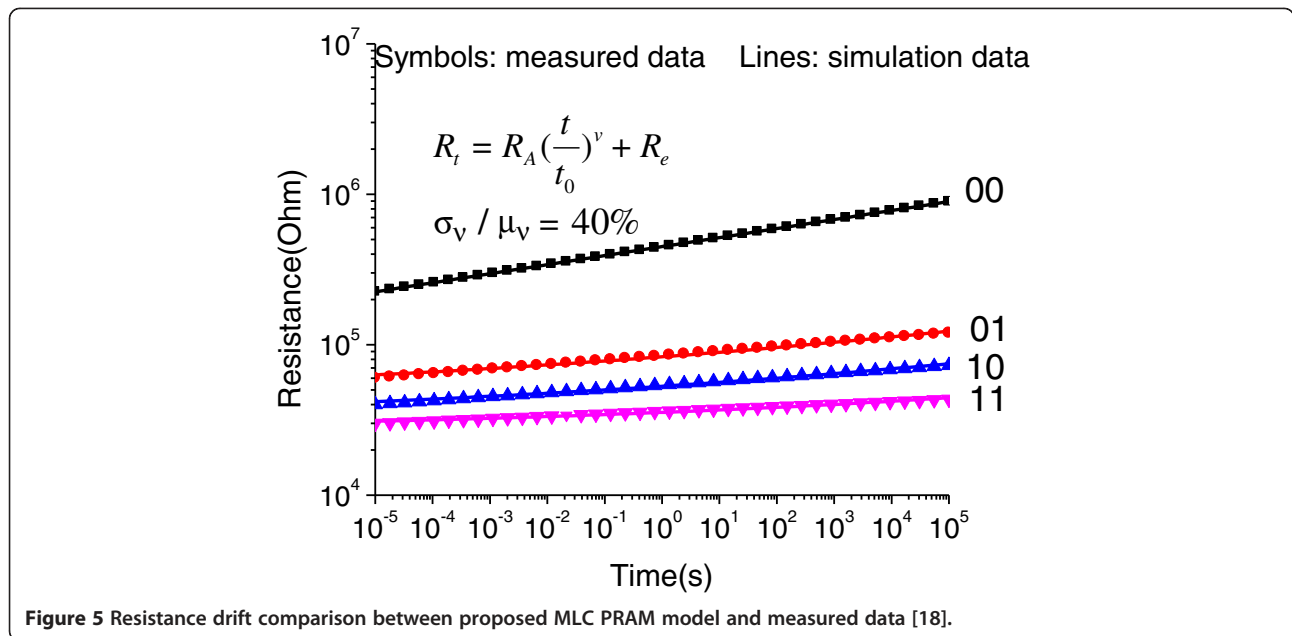


**Figure 4 Resistance distribution of four states in 2-bit MLC PRAM.** (a) Distribution in nominal mode. (b) An example of errors caused by the ‘01’ resistance shift.





data are stored in memory between two consecutive writes. Thus, the storage time has to be less than the data retention time. For PRAM, data retention depends on the stability of the resistance in the crystalline and amorphous phases. While the crystalline phase is fairly stable with time and temperature, the amorphous phase suffers from resistance drift and spontaneous crystallization. Initially, the resistance increases due to structure relaxation (SR) [10], a phenomenon seen in amorphous chalcogenides and related to the dynamics of the intrinsic traps. Eventually, crystallization in the amorphous phase results in a drop in resistance and thereby loss of data in the cell. SR of the amorphous phase affects both resistance and threshold voltage of amorphous phase [21]. However, since the read region of the voltage is usually below the threshold voltage, only resistance drift is studied in this article. Resistance drift results in soft errors as will be described shortly.

Hard errors occur when the data value stored in one cell cannot be changed in the next programming cycle. There are two types of hard errors in PRAM: stuck-RESET failure and stuck-SET failure [20]. Stuck-SET or stuck-RESET means that the value of stored data in PRAM cell is stuck in SET or RESET state no matter what value has been written into the cell. These errors increase as the number of programming cycles increases.

Data disturb, known as proximity disturb, can occur in a cell in RESET state if surrounding cells are repeatedly programmed. In this case, the heat generated during the programming operation diffuses from the neighboring cells and accelerates crystallization. Another type of disturb, read disturb, occurs when a cell is read many times. This type of disturb is dependent upon the

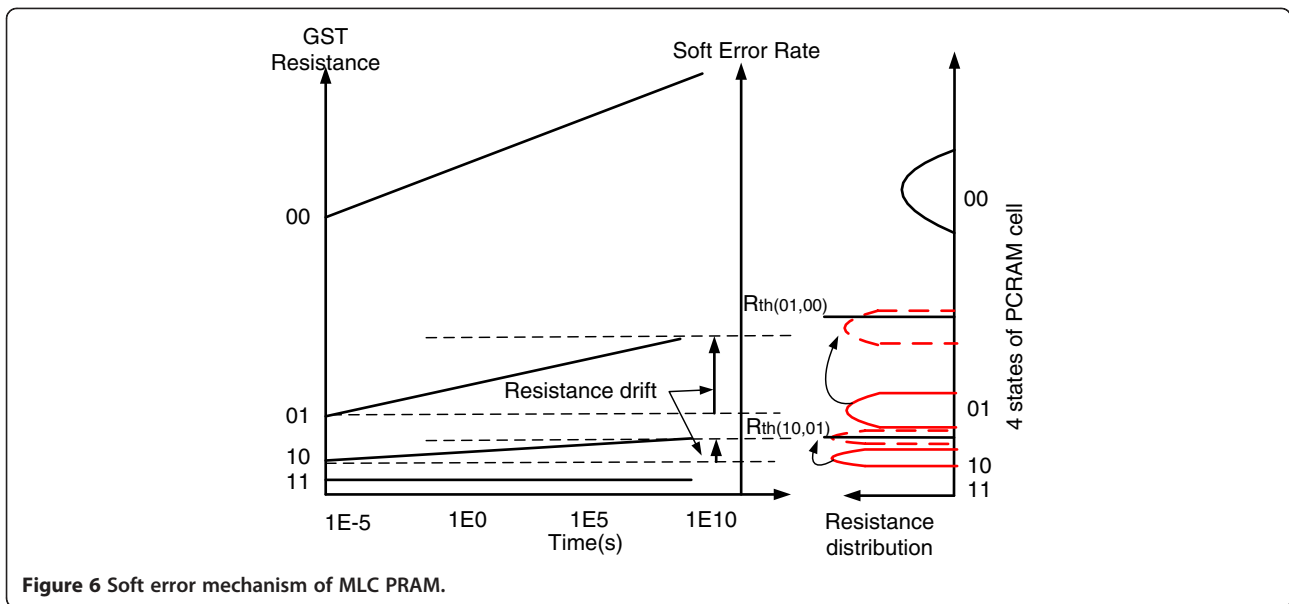
applied cell voltage and ambient temperature. Both these types of disturb are not as prevalent and so in the rest of this section we focus on the effects of data retention and cycling endurance on the error rate.

The resistance distribution of a 2-bit MLC PRAM is shown in Figure 4a. The distributions of the intermediate states ('01' and '10') are shaped by the multiple-step programming strategy. There are three threshold resistances  $R_{th(11,10)}$ ,  $R_{th(10,01)}$ , and  $R_{th(01,00)}$  to identify the boundaries between the four states. These resistances can be changed by tuning the reference current of the differential current amplifier during read sensing as has been demonstrated in MLC Flash memory architectures in [22]. Due to the change in the material characteristics such as SR or re-crystallization, the resistance distribution of logical states shifts from the initial position. Memory cells fail when the distribution crosses the threshold resistance level as shown in Figure 4b; the error rate is proportional to the extent of overlap. In this article, we assume that the initial resistance distribution is Gaussian. The mean values of the resistances have been listed in Table 1; the deviation is 0.17 as used in [11].

According to the proposed programming strategy, the resistances of intermediate states are always set back to the initial values in the next programming cycle. Thus, the effect of this resistance drift is cancelled in the next programming cycle and it only causes soft errors. A

**Table 2 Parameters of resistance drift model**

	State 00	State 01	State 10	State 11
$R_A$	225000	48319	15319	10026
$R_e$	0	3533	265	18



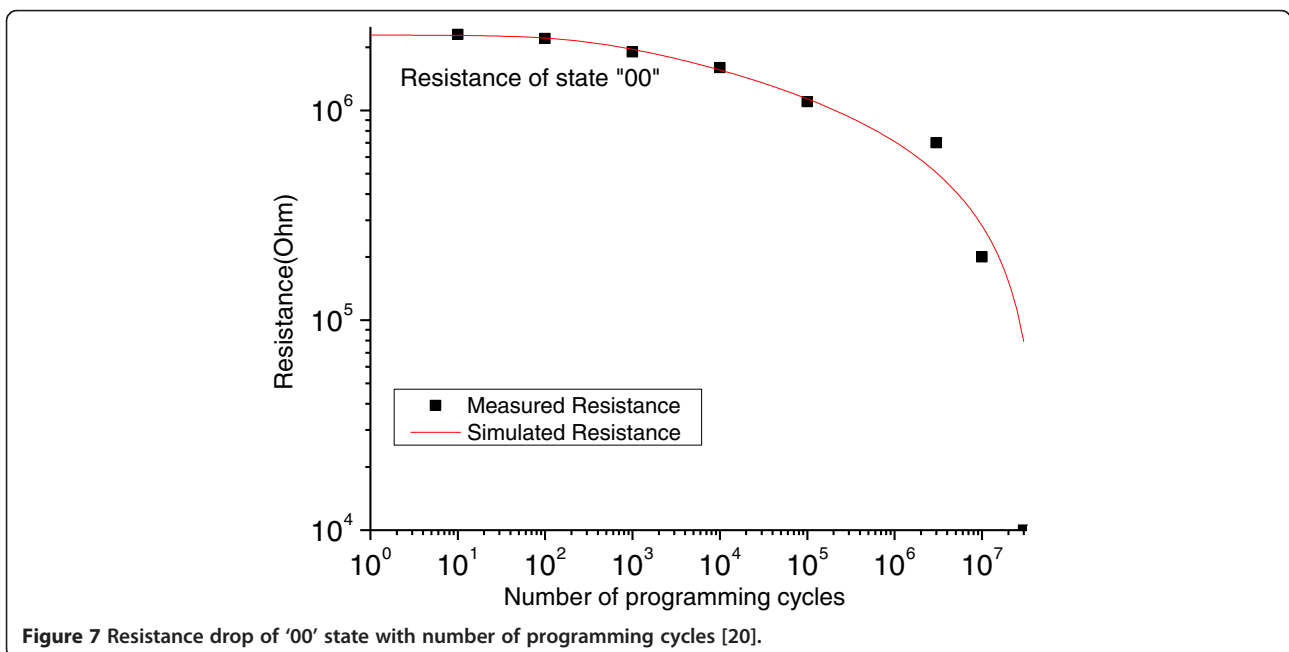
simple model has been built to model resistance drift due to SR. Since  $R_A$  represent the amorphous active region exclusively, let  $R_e$  represent the impact of all the other resistances. Then, MLC PRAM time-dependent resistance is given by

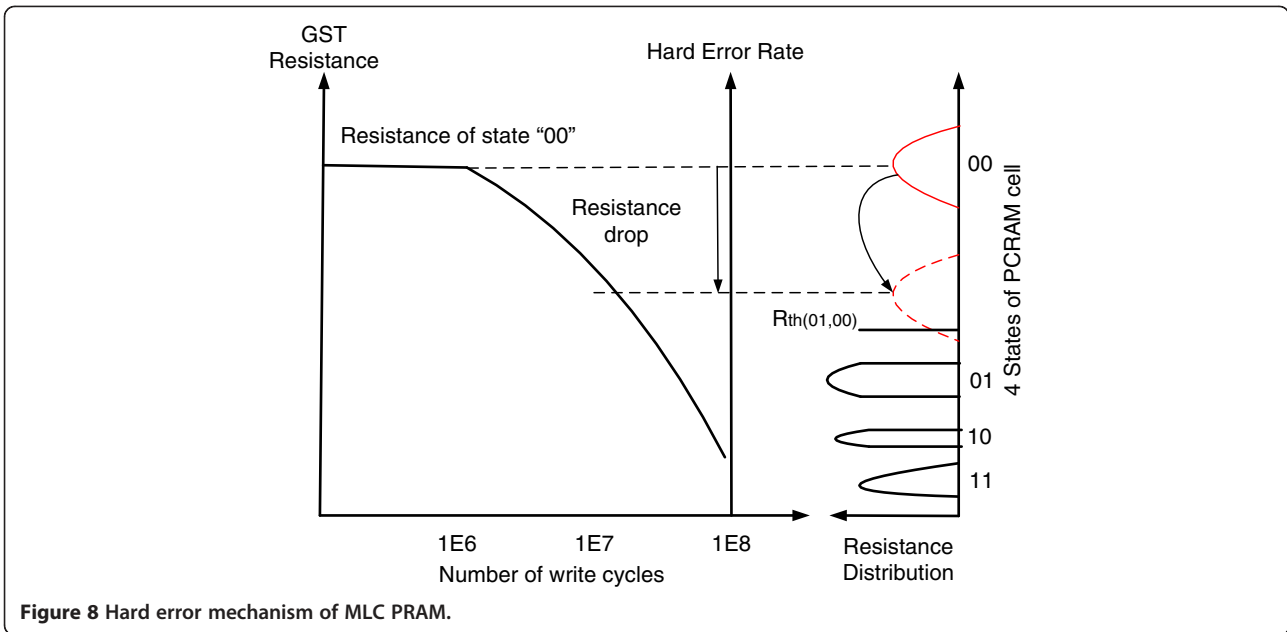
$$R_t = R_A \left( \frac{t}{t_0} \right)^\nu + R_e \quad (1)$$

where  $R_A$  and  $R_e$  are varying and  $\nu$  is the resistance drift coefficient, which is constant for all the intermediate states. Measured data from [23] almost match the

simulated data as shown in Figure 5. Note that in [11], is used to approximately fit measured data for short time periods. However, for longer time periods, this model is not accurate and gives a lower estimated soft error rate. In this article,  $\nu$  is set to 0.11, a typical value which has been used in [11,21], and the standard deviation to mean ratio is 40% as defined in [11]. Based on the initial resistance in Table 1,  $R_A$  and  $R_e$  in this article are listed in Table 2.

Figure 6 describes the two mechanisms that result in soft errors. The error rate due to state '10' crossing  $R_{th(10,01)}$  and state '01' crossing  $R_{th(01,00)}$  depends on the distributions of the resistances of states '10' and

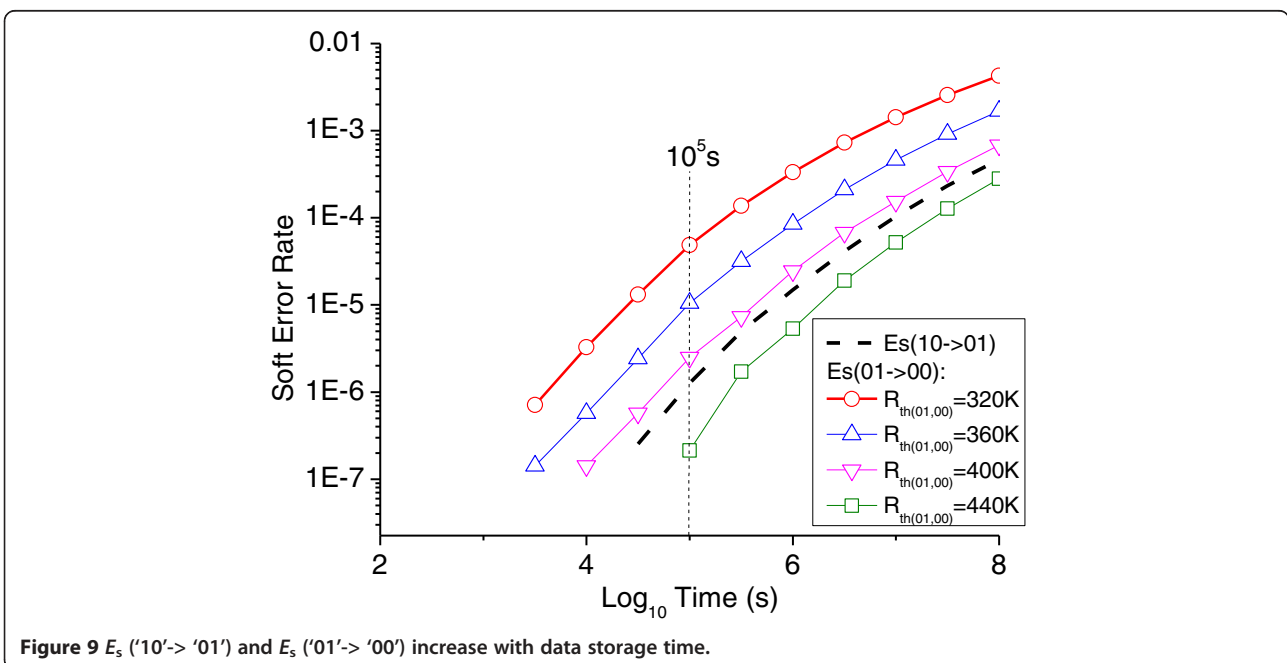




'01' and the values of  $R_{th(10,01)}$  and  $R_{th(01,00)}$ . Increasing  $R_{th(01,00)}$  results in larger reduction in the soft error rate, as will be shown later.

Stuck-SET failure is due to repeated cycling that leads to Sb enrichment at the bottom electrode [21]. Sb rich materials have a lower crystallization temperature leading to data loss and crystallization of the region above the bottom electrode at much lower temperatures than the original material composition. As a result, the bottom electrode cannot heat the GST material

sufficiently, and the resistance is lower than the desired level of reset state. The resistance drop can be analyzed as Ge density distribution change, similar to the trap density change for resistance drift. The resistance reduction is a power function of the number of programming cycles  $N$  and is given by  $\Delta R = aN^b$ . Figure 7 compares the resistance drop model of '00' state with measured data from [24]. It shows that this model is fairly accurate; here  $a$  equals 151609 and  $b$  equals 0.16036.





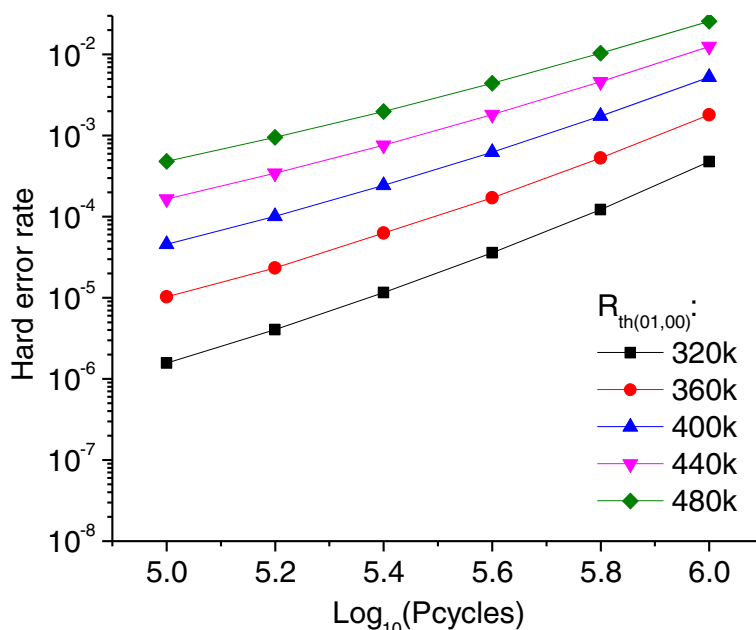


**Figure 10** Hard error rate as a function of  $R_{th(01,00)}$  and number of programming cycles ( $P_{cycles}$ ).

In a stuck-RESET failure, the device resistance suddenly and irretrievably spikes, entering a state that has much higher resistance than the normal RESET state. Stuck-RESET can also be caused by over programmed current [20]. Higher programming current results in larger amorphous volume, which takes more time to become crystalline, shows higher resistance than desired value after a SET operation.

For SLC PRAM, most of the failures are stuck-SET failure. Since the resistances of intermediate states of MLC PRAM are guaranteed by read and verify steps in the write operation, the hard error mechanism of MLC PRAM is the same as that of SLC PRAM. Figure 8 shows how the resistance of '00' state drops over time. When the resistance distribution of state '00' crosses  $R_{th(10,01)}$ , hard errors occur.

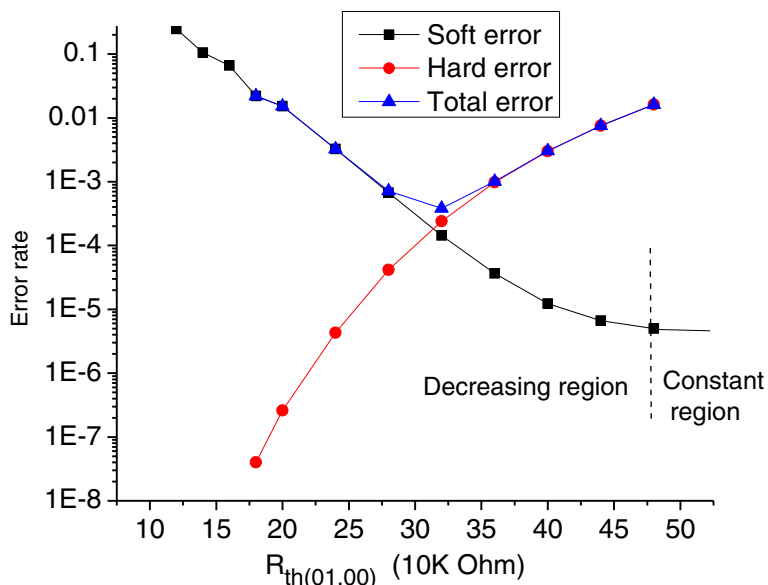


**Figure 11** Total error (hard and soft) rate of 2-bit MLC PRAM. Soft error rate is calculated at 10<sup>5</sup> s, hard error rate is calculated at 10<sup>6</sup> cycles.

**Circuit-level techniques for reducing soft and hard errors**

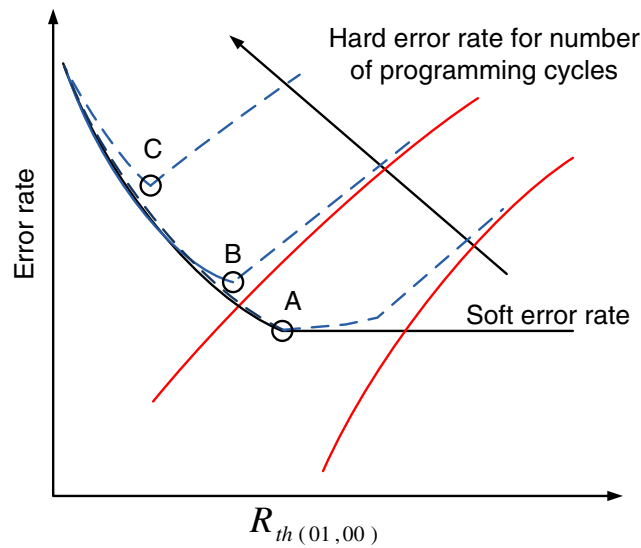
In the previous section, we have shown that the soft error rate increases with data storage time and that the hard error rate increases with the number of programming cycles. In this section, we show how the error rate can be controlled by tuning the threshold resistance  $R_{th}$  (00,01) for a specific data storage time. Recall that threshold resistance can be tuned by changing the current reference of the sense amplifier. Data storage time is set

to  $10^5$  s, which is typical of storage systems such as those for daily backup.

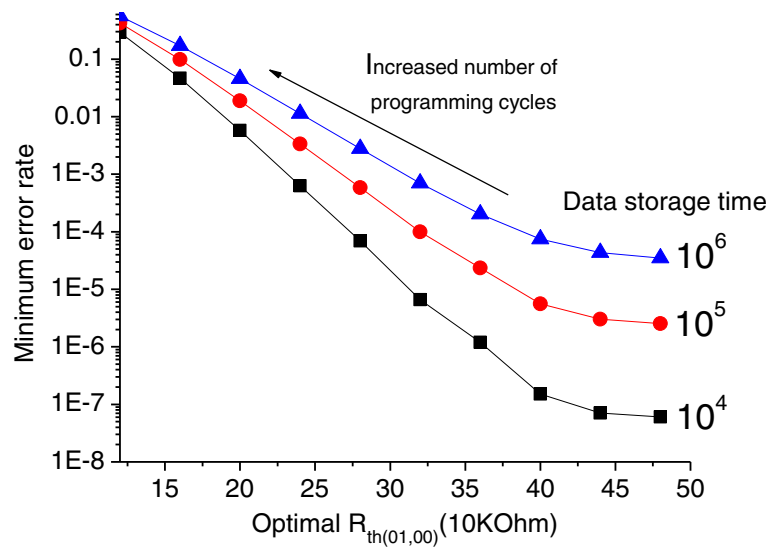
However, if data storage time distribution is known *a priori*, then a better estimate of this time can be used to derive the threshold resistance.

**Soft error rate**

The soft error rate of 2-bit MLC PRAM is a function of the resistance drift of '01' to '00' state,  $E_s$  ('01' -> '00'), and



(a)



(b)

**Figure 12 Demonstration of error rate as a function of number of programming cycles and threshold resistance.** (a) Total error rate as function of number of programming cycles for a specific data storage time. (b) Total minimized error rate as a function of optimal threshold resistance for three data storage time values.

the resistance drift of '10' to '01' state,  $E_s$  ('10'-'>'01'). While  $E_s$  ('01'-'>'00) depends on the value of  $R_{th(01,00)}$ ,  $E_s$  ('10'-'>'01) depends on the value of  $R_{th(10,01)}$ .

Figure 9 describes how the soft error rate increases with data storage time for different values of  $R_{th(01,00)}$ . Here,  $R_{th(01,10)}$  is set as the middle value between resistances of '01' and '10' states, which is 30.5K in this case. Tuning this resistance is difficult because of the close spacing between the distributions of the '01' and '10' states. In this scenario, however,  $R_{th(01,00)}$  has a much

higher impact on the total soft error rates; as  $R_{th(01,00)}$  increases, the soft error rate reduces.

In order to counteract the effect of resistance drift, dynamic  $R_{th(01,00)}$  and  $R_{th(10,01)}$  tuning has been proposed in [11]. Here, a time tag is used to record the storage time information for each memory block or page and this information is used to determine the threshold resistance that minimizes the BER. The technique in [11] considers the effect of resistance drift on soft errors. The threshold resistance value affects the hard error rate as well and so the

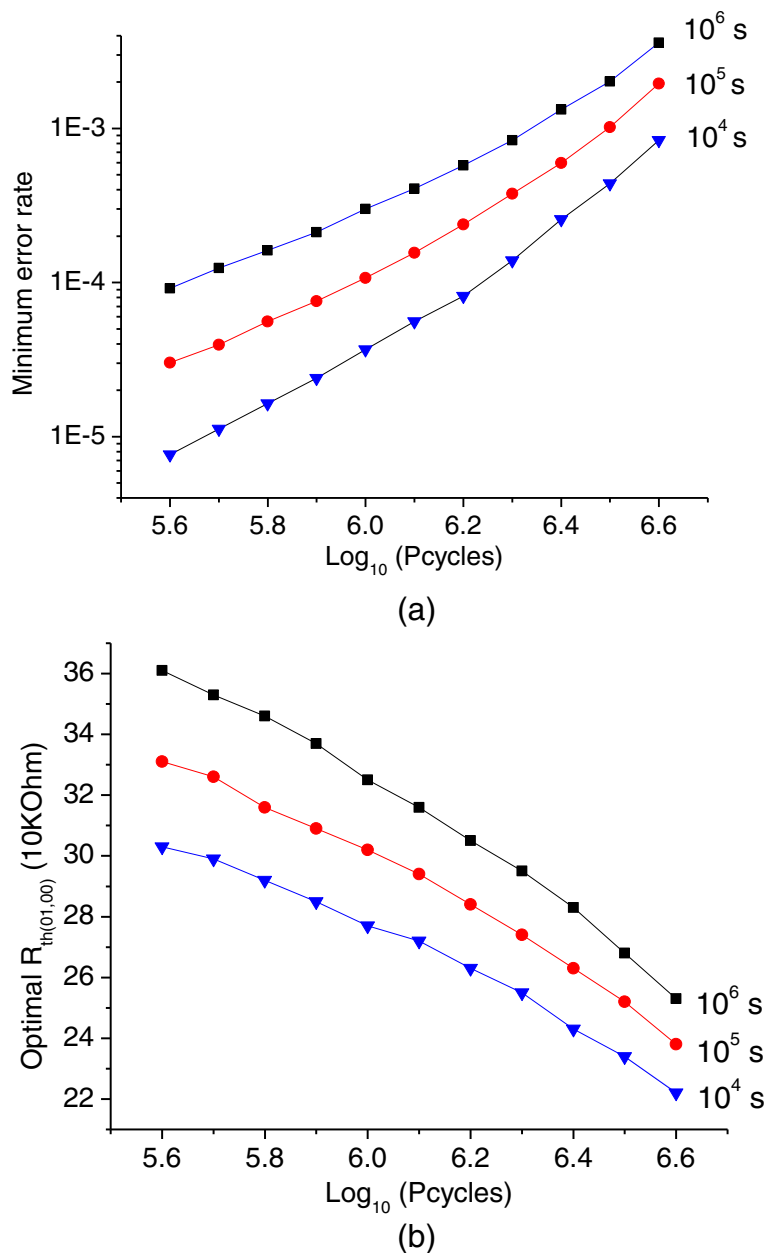


**Figure 13** Demonstration of the gradient of different data storage time. (a) Minimum total error rate as a function of numbers of programming cycles for different data storage times. (b) Optimal threshold resistance.

choice of threshold resistance has to be determined by both soft and hard error rates as will be described next.

**Hard error rate**

The hard error rate of 2-bit MLC PRAM is due to the resistance drop of ‘00’ state to the ‘01’ state as shown in Figure 7. It is a function of  $R_{th(01,00)}$ , and the resistance distribution of state 00. Due to multiple pulse write strategy for intermediate states, there is no resistance drop from ‘01’ state to ‘10’ state, and thus  $R_{th(10,01)}$  has no impact on the hard error rate.

Figure 10 shows the hard error rate as a function of the number of programming cycles for different values of  $R_{th(01,00)}$ . We see that for a specific  $R_{th(01,00)}$ , the hard error rate increases exponentially with number of programming cycles. It also shows that for a specific number of programming cycles, lower threshold resistance results in lower hard error rate. Therefore, lower  $R_{th(01,00)}$  results in fewer hard errors.

**Total error rate**

Consider a scenario where the number of programming cycles is  $10^6$  and the data storage time is  $10^5$  s. Since

both the hard error and soft error rates are a function of  $R_{th(01,00)}$ , we combine the two error rates in Figure 11 and present them as a function of  $R_{th(01,00)}$ . We see that while the hard error rate increases monotonically, the soft error rate curve decreases at first and then becomes constant. Soft error rate keeps decreasing till a critical  $R_{th(01,00)}$  is reached, which is 440K in this case. It then maintains a constant value which is determined by the error rate  $E_s$  (‘10’-> ‘01’). From the plot we see that the lowest total error occurs at  $R_{th(01,00)}$  of 320K.

Figure 12 generalizes the above procedure. Figure 12a shows how for a specific data storage time (given by soft error curve), the optimal  $R_{th(01,00)}$  reduces as the number of programming cycles increases. Figure 12b provides the lowest error rate values as a function of optimal  $R_{th(01,00)}$  for three data storage times. As the data storage time increases, the error rate increases, as expected.

Figure 13a shows that for a fixed data storage time, as the number of cycles increases, the total BER increases. Figure 13b shows the corresponding values of  $R_{th(01,00)}$ . The advantage of threshold resistance tuning is that it provides an easy way of achieving the lowest possible error rate considering both soft and hard errors. From Figure 11,

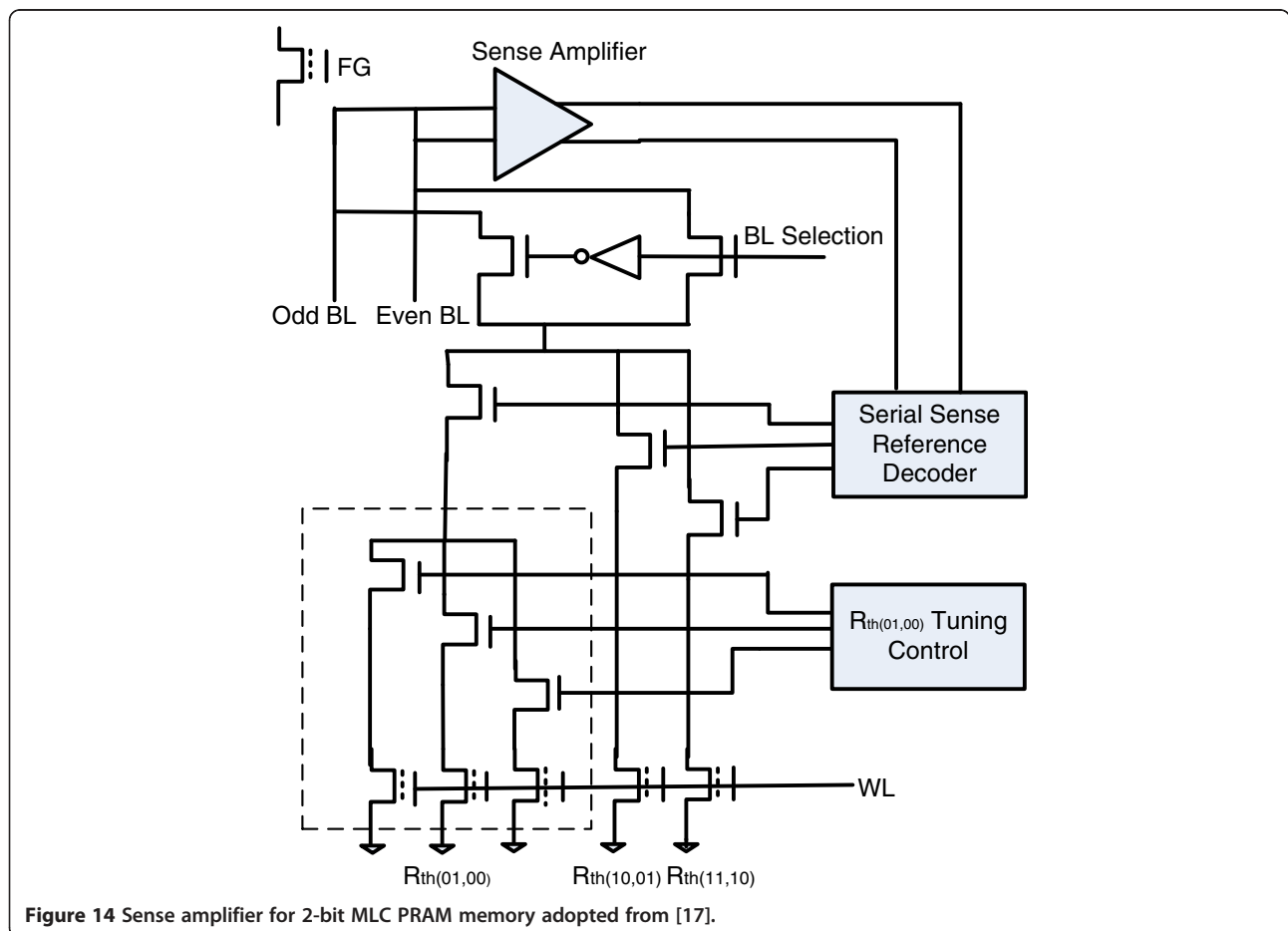


**Figure 14** Sense amplifier for 2-bit MLC PRAM memory adopted from [17].

we can see that for a specific case of 2-bit MLC PRAM, in which the effective data storage time is  $10^5$  s at  $10^6$  programming cycles, the total BER has been reduced from  $10^{-2}$  to about  $10^{-4}$ . Reducing the error rate any further with circuit-level tuning is costly. In “ECC schemes” section, we show how ECC techniques can be used in conjunction with threshold resistance tuning to achieve significantly lower BER with much lower overall cost.

**Tuning threshold resistance**

Figure 14 shows how the serial sense amplifier used in the MLC Flash architecture [25] can be used to support varying threshold resistance for 2-bit MLC PRAM. The floating gates (FG) in the access transistors (controlled by WL) are used to set the values of  $R_{th(01,00)}$ ,  $R_{th(10,01)}$ , and  $R_{th(11,10)}$ . The different resistances result in different reference currents in this circuit. The three reference resistances are selected by the sense reference decoder in a serial order to determine whether the bits that were read out are ‘00’, ‘01’, ‘10’, or ‘11’. Further tuning of  $R_{th(01,00)}$  can be achieved by introducing a second level of selection transistors to select the specific FG transistor. The  $R_{th(01,00)}$  tuning block makes the selection based on the optimal  $R_{th(01,00)}$  value. Recall that this value changes with data storage time and number of programming cycles and so dynamic tuning is desirable. Figure 14 shows a three-FG design for  $R_{th(01,00)}$ ; for finer tuning, more FGs are required.

**STT-RAM reliability**

In this section, we describe the basic structure of the STT-RAM cell including its read/write operations (see the next section), sources of its errors (see “STT-RAM error model” section), and circuit-level techniques to reduce them (see “Circuit-level techniques for reducing error” section).

**Background**

In STT-RAM, the resistance of the MTJ determines the logical value of the data that are stored. MTJ consists of a thin layer of insulator (spacer-MgO) about approximately 1-nm thick sandwiched between two layers of ferromagnetic material [5]. Magnetic orientation of one layer is kept fixed and an external field is applied to change the

**Table 3 Device parameters of STT-RAM**

	Nominal	Variance
Transistor channel length(nm)	32	5%
Transistor channel width (nm)	96, 128, 160	5%
Transistor threshold (RDF)	0.4 V	$\sigma_{VT}=40$ mV
$R_p$ (P)	2.25K	Approximately 6%
$R_{AP}$ (AP)	4.5K	Approximately 6%
MTJ initial angle	0	$0.1\pi$

orientation of the other layer. Direction of magnetization angle (P or AP) determines the resistance of MTJ which is translated into storage; P corresponds to storage of bit 0 and AP corresponds to storage of bit 1. Low resistance (P) state is accomplished when magnetic orientation of both layers is in the same direction. By applying external field higher than critical field, magnetization angle of free layer is flipped by  $180^\circ$  which leads to a high resistance state (AP). The difference between the resistance values of P and AP states is called tunneling magneto-resistance (TMR) which is defined as  $TMR = \frac{R_{AP}-R_p}{R_p}$  where  $R_{AP}$  and  $R_p$  are the resistance values at AP and P states. Increasing the TMR ratio makes the separation between states wider and improves the reliability of the cell [7]. Figure 15 describes the cell structure of an STT-RAM and highlights the P and AP states.

A physical model of MTJ based on the energy interaction is presented. Magnetization angle of the free layer is determined based on the dimensions of MTJ and the external field applied. Energies acting in MTJ are Zeeman, anisotropic, and damping energy [25]. These energy types determine the change in magnetic orientation, alignment of the magnetization angle along the fixed axis and are used to form the Landau–Lifshitz–Gilbert equation. The stable state of MTJ corresponds to minimum total energy. State change of MTJ cell can be derived by combining these energy types:

$$\frac{d\vec{M}}{dt} = -\mu_0 \cdot M_s \cdot \vec{H} + \frac{\alpha}{M_s} \cdot \vec{M} \times \frac{d\vec{M}}{dt} + K \sin\theta \cos\theta \tag{2}$$

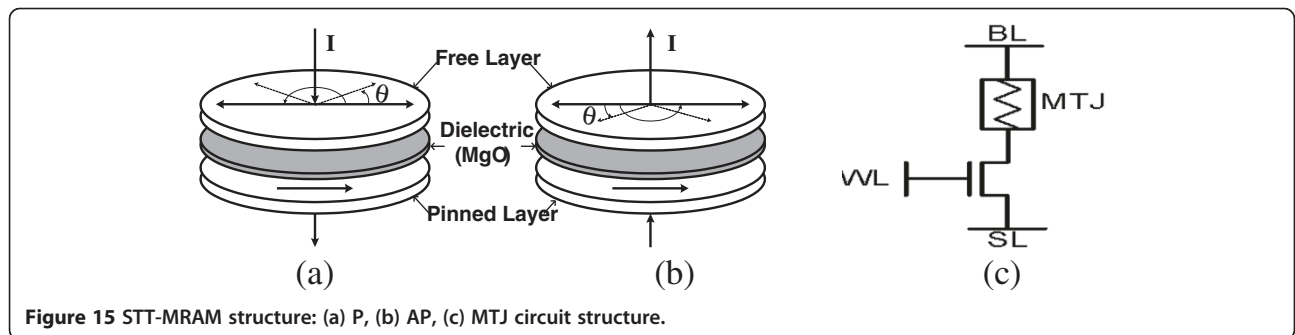


**Figure 15 STT-MRAM structure: (a) P, (b) AP, (c) MTJ circuit structure.**

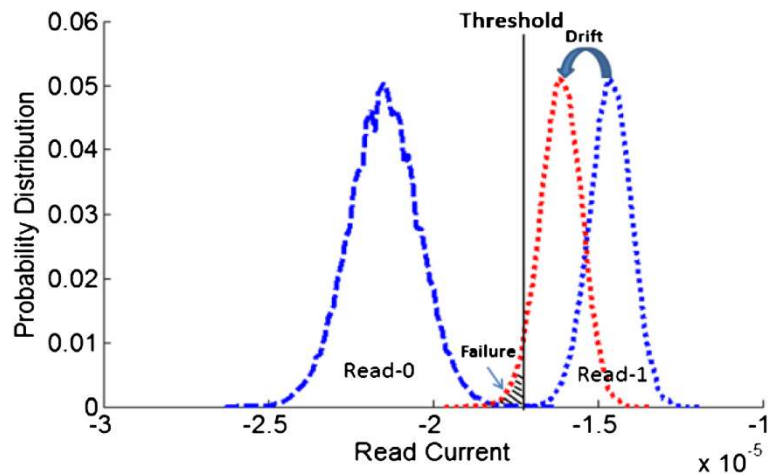


**Figure 16** Failures occur when the distributions of read-0 and read-1 current overlap.

where  $\vec{M}$  is magnetic moment,  $\mu_0$  is vacuum permeability,  $\alpha$  is damping constant. Such an equation can be modeled using Verilog-A to simulate the circuit characteristics of STT-RAM. For instance, differential terms are modeled using capacitance while Zeeman and damping energy are described by voltage-dependent current source. The voltage of the capacitor indicates the evaluated state (magnetization angle) which is further translated to resistance of MTJ.

Consider the cell structure consisting of an access transistor in series with the MTJ resistance illustrated in Figure 15c. The access transistor is controlled through WL, and the voltage levels used in BL and SL lines determine the current which is used to adjust the magnetic field. There are three modes of operation for an STT-RAM: write-0, write-1, and read. We distinguish between

write-0 and write-1 because of the asymmetry in their operation. In general, directions of the current during write-0 and read operation are the same, while the magnitude of the current is fairly high (approximately 10 $\times$ ) during the write operation. For read operation, current (magnetic field) lower than critical current (magnetic field) is applied to MTJ to determine its resistance state. Low voltage (approximately 0.1 V) is applied to BL, and SL is set to ground. When the access transistor is turned on, a small current passes through MTJ whose value is detected based on a conventional voltage sensing or self-referencing schemes [26]. During write operation, BL and SL are charged to opposite values depending on bit value that is to be stored. During write-0, BL is high and SL is set to zero, whereas during write-1, BL is set to zero and SL is set to high. The asymmetric structure of write-0 and

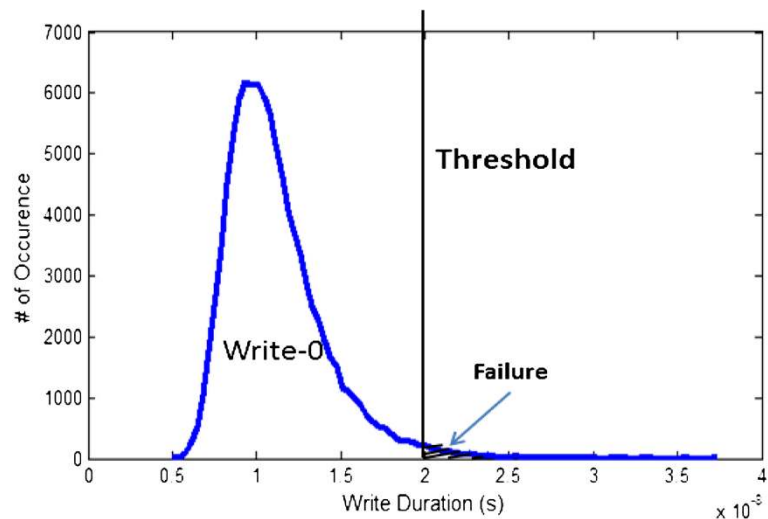


**Figure 17** Distribution of write time during write-0. Failure occurs when the write-0 distribution crosses the threshold value.



**Table 4 BERs of a single STT-RAM cell**

Read ( $V_{\text{read}} = 0.1 \text{ V}$ )	Write (pulse width = 25 ns)	0	1
0	1	0	1
Approximately $10^{-5}$	Approximately $10^{-5}$	Approximately $4 \times 10^{-5}$	

write-1 operations motivates SL line to be higher than nominal during write-1 so that both operations generate comparable write-current. Such a circuit technique is elaborated in the next section.

**STT-RAM error model**

There are several factors that affect the failure in STT-RAM memories: access transistor manufacturing errors such as those due to RDFs, channel length, and width modulations, geometric variations in MTJ such as area and thickness variation, and thermal fluctuations that are modeled by the initial magnetization angle variation [15]. Note that all these variations cause hard errors.

Apart from errors that are caused by process variations, MTJ also suffers from time-dependent reliability

issues. MTJ structure consists of a very thin insulating layer (approximately 1 nm) and voltage across MTJ can approximately be 0.6–1 V. This results in a very high electric field across the thin insulator (approximately 10 MV/cm) which can cause time-dependent dielectric breakdown (TDDB). With high scaling, the electric field across insulating layer rises, thereby increasing the possibility of TDDB.

Next we consider the effect of key process variation factors on the error rate. The effect of RDF on threshold voltage is typically modeled with an additive independent and identically distributed (i.i.d.) Gaussian distribution. Variance of threshold voltage of a MOSFET is proportional to  $\sigma_{V_T} \propto \frac{EOT}{L_t \times W_t}$ , where EOT is oxide thickness, and  $L_t$  and  $W_t$  are length and width of the

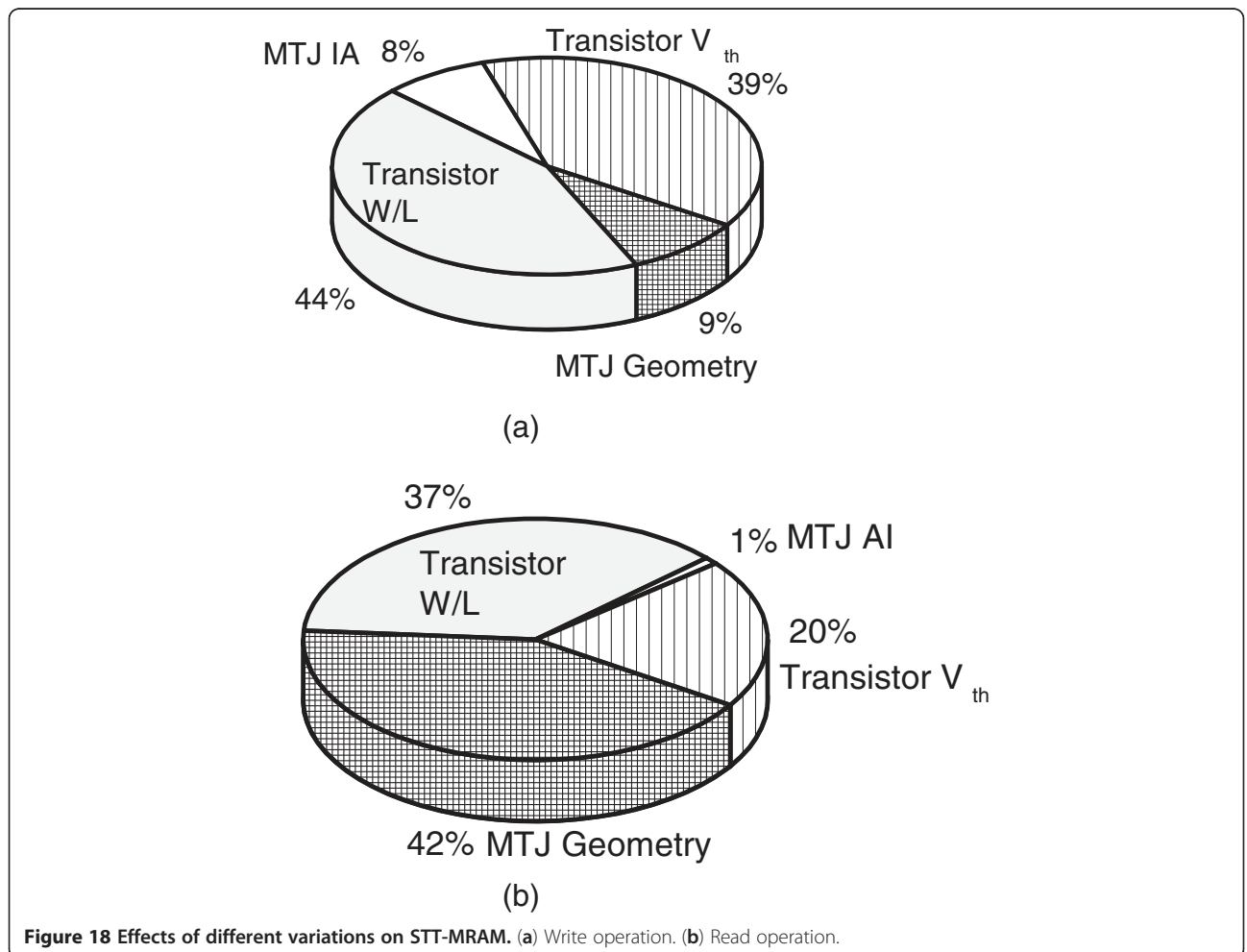


**Figure 18** Effects of different variations on STT-MRAM. (a) Write operation. (b) Read operation.

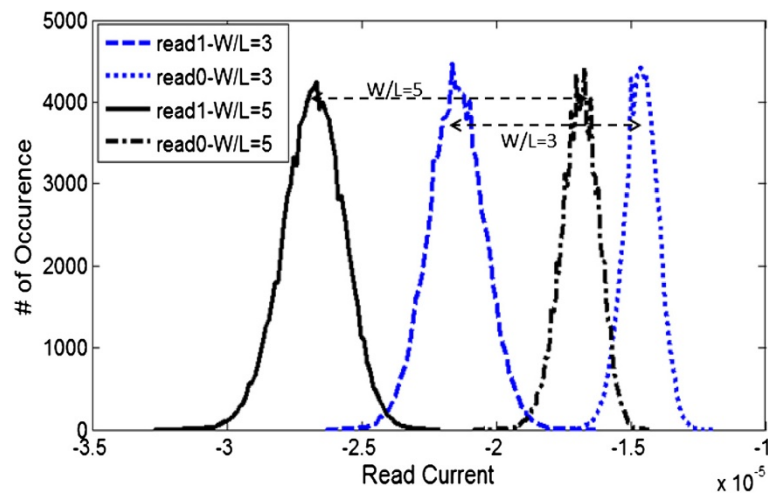


**Figure 19** Distribution of read current for different access transistor sizes.

transistor, respectively. For 32 nm,  $\sigma_{VT}$  is approximately between 40 and 60 mV [27]. We model CMOS channel length and width variation using i.i.d. Gaussian distribution with 5% variation. These variations induce change in the drive current of the transistor which results in increase on variation in both read and write operations. Variation in tunneling oxide thickness  $t_{OX(MTJ)}$  and surface area  $A_{MTJ}$  of MTJ are the main causes behind the random resistance change in MTJ material. Resistance of the MTJ is proportional to  $\propto (1/A_{MTJ})e^{t_{ox}(MTJ)}$  [13]. In our simulations, we set the nominal values of  $(R_p)$  to 2.25K and  $(R_{AP})$  to 4.5K and modeled the variations using i.i.d. Gaussian distribution with 2% variance for thickness and 5% variance for the area [13]. Furthermore, initial magnetization angle of the MTJ affects the duration of the write operation, since it induces extra

resistance when the angle is not aligned properly at the initial state. Such variation is also modeled using i.i.d. Gaussian distribution with 0.1 radian variance [7]. The nominal values and variance of the device parameters are listed in Table 3. We consider 40 mV variation for RDF when width of 128 nm which is equivalent to  $W/L = 4$  and scaled it for different  $W/L$  ratios.

**Errors in read and write operations**

The reliability of an STT-RAM cell has been investigated by several researchers. While Chatterjee et al. [7] studied the failure rate of a single STT-RAM cell using basic models for transistor and MTJ resistance, process variation effects such as RDF and geometric variation were considered in [15,28]. In this section, we also present the effects of process variation and geometric variation. We add the variation effects to the nominal HSPICE model

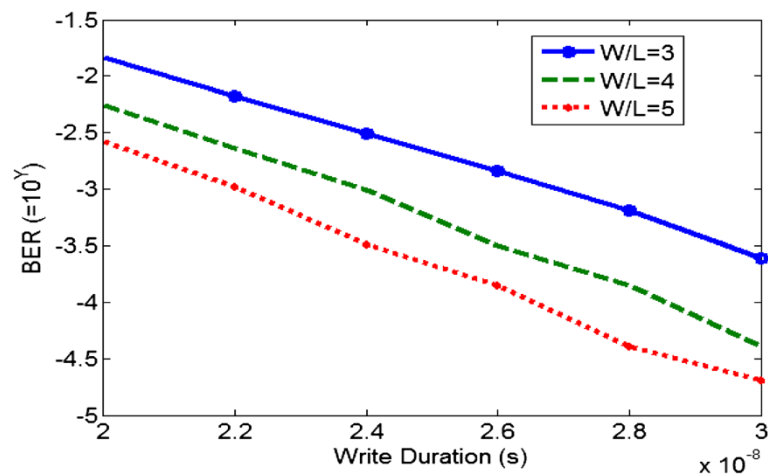


**Figure 20** BER versus write pulse duration for different  $W/L$  ratios.

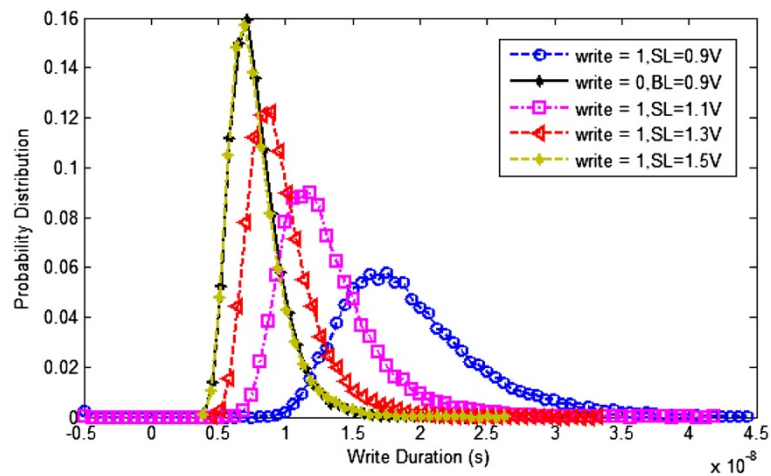


**Figure 21** Probability distribution of write-0 and write-1 for different values of SL voltage.

of STT-RAM and use Monte Carlo simulations to generate the error rates caused by each variation.

**Read operation** During read operation, BL is set to 0.1 V, SL is set to ground and the stored value is determined based on the current passing through the MTJ. Figure 16 describes the read current distributions for 32 nm technology (nominal voltage is 0.9 V) for transistor  $W/L = 4$ . Threshold current value is used to distinguish between two states (read-0 and read-1). Typically, there are two main types of failures that occur during the read operation: read disturb and false read. Read disturb is the result of the value stored in the MTJ being flipped because of large current during read. False read occurs when the current of P (AP states) crosses the threshold value of the AP (P) state as illustrated in Figure 16. In our

analysis, we find that the false read errors are dominant during the read operation, thus we focus on false reads in the error analysis.

**Write operation** During write 0, BL is high and SL is set to zero whereas during write-1 BL is set to zero and SL is set to high. Figure 17 illustrates the write-0 time distribution of an STT-RAM cell for access transistor size of  $W/L = 4$ ,  $BL = 0.9$  V,  $SL = 0$ . We observe that such a distribution has a long tail unlike a Gaussian distribution. During write operation, failures occur when the distribution of write latency crosses the predefined access time as illustrated in Figure 17. Write-1 is more challenging for an STT-RAM device due to the asymmetry of the write operation. During write-1, access transistor and MTJ pair behaves similar to a source

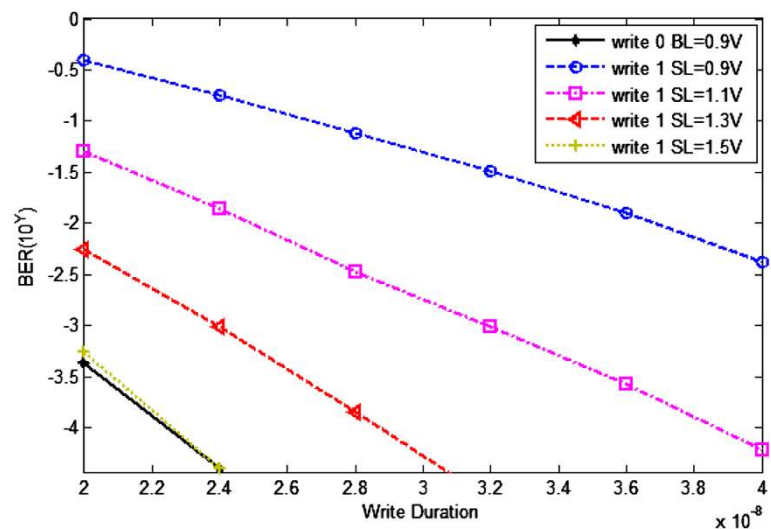


**Figure 22** BER versus write pulse duration for different values of SL voltage.

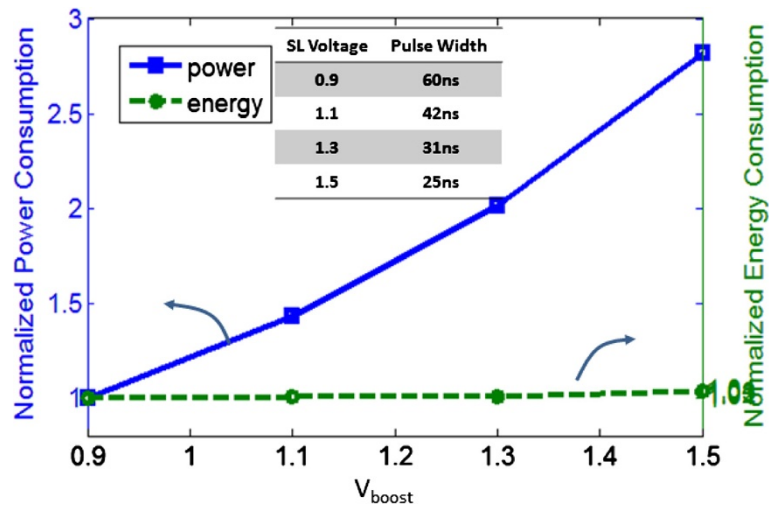


**Figure 23** Power and energy consumption for different values of boosted voltage and write pulse width.

follower which increases the voltage level at the source of the access transistor and reduces the driving write current. Such a behavior increases the time required for a safe write-1 operation.

Table 4 shows the BER for read and write operations of STT-RAM at nominal conditions corresponding to  $V_{dd} = 0.9V$ , write pulse = 25ns,  $V_{read} = 0.1V$  and access transistor size of  $W/L = 4$ . Write-1 has very high BER compared to write-0 which has a BER of  $10^{-5}$ . The effect of such asymmetry in write operation on system reliability has also been presented in [13,28].

The variation impacts of the different parameters are presented in Figure 18 for read and write operations. To generate these results, we changed each parameter one at a time and did Monte Carlo simulations to calculate the contribution of each variation on the overall error rate. We see that variation in access transistor size is very effective in shaping the overall reliability; it affects the read operation by 37% and write operation by 44% with the write-0 and write-1 having very similar values. The threshold voltage variation affects the write operation more than the read operation. Finally, the MTJ

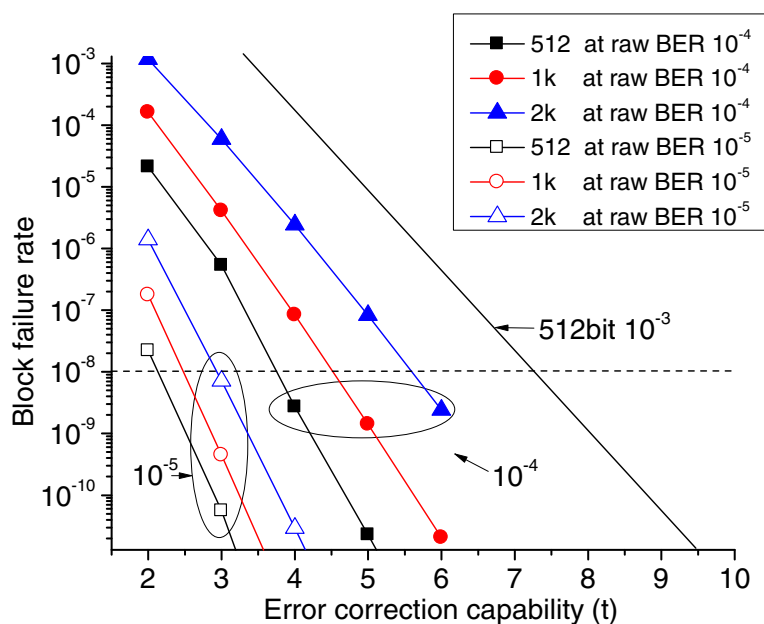


**Figure 24** BFR versus ECC correction capability for  $N = 512, 1024,$  and  $2048$  bits for raw BER =  $10^{-4}$  and  $10^{-5}$ .

geometry variation is more important in determining the read error rate as illustrated in Figure 18b.

**Circuit-level techniques for reducing error**

In this section, we show how  $W/L$  sizing of access transistor, voltage boosting, and pulse width adjustment can be used to improve the reliability of the STT-RAM cell. Access transistor sizing has been investigated in [7,13], effect of process variation as well as write pulse width has been studied in [13,14,28] and voltage boosting of WL has been considered in [13,29]. Here, we also study the read reliability and investigate the effect of combination of write pulse width and voltage boosting on the write reliability.

**Effect of  $W/L$  of access transistor**

The width of the access transistor has two effects on the read current distribution: it reduces the effect of RDF variation and improves the reliability by increasing the distance between the mean of the read-0 and read-1 distributions. Figure 19 illustrates this phenomenon by plotting the read current distributions for three  $W/L$  ratios of the access transistor. Thus based on the  $W/L$  ratios we can choose the threshold value that maximizes the detection probability, which in return minimizes the BER. For instance, when  $W/L=3$ ,  $BER = 0.7 \times 10^{-4}$ ; it reduces to  $BER = 2.5 \times 10^{-5}$  when the size increases to  $W/L=5$ . Even though increasing  $W/L$  improves the reliability for the read operation, it reduces the cell density and increases the power consumption.

We also looked at the effect of  $W/L$  ratio on write failure. When  $W/L$  ratio of the access transistor increases, its current driving capability is enhanced and the necessary time duration for a successful write operation is reduced. Figure 20 illustrates the BER versus write time duration of a write-1 operation for three different values of  $W/L$ .

**Table 5 ECC scheme for STT-RAM and PRAM to achieve the target BFR**

	512 bits	1024 bits	2048 bits
STT-RAM	BCH(542,512)	BCH(1057,1024)	BCH(2084,2048)
PRAM	BCH(552,512)	BCH(1079,1024)	BCH(2120,2048)

**Effect of voltage boosting**

Gate level (WL) voltage boosting has been investigated in [13,29] to reduce the write-1 latency of STT-RAM. It is an effective way of increasing the drive current of access transistor which leads to reduction in latency. However, WL boosting requires separate WLs for write-0 and write-1 operations. Two-step writing, erase/program schemes have been proposed to overcome the limitations; however, all the schemes incur extra latency or energy consumption. We propose boosting SL during write operation to improve the write-1 reliability. This method enables reduction of the pulse duration for write-1 operation while incurring very small overhead. Figure 21 illustrates the latency distribution of write-1 operation when access transistor size is  $W/L = 4$ , BL is set to zero and SL varied from 0.9 (nominal) to 1.5 V. We see that boosting SL voltage level over nominal voltage level reduces the average latency and variation of the write-1 operation. The distributions of write-0 at nominal voltage and write-1 when the supply voltage is boosted up to 1.5 V have almost identical characteristics. If the pulse width for both write-0 and write-1 operations are the same, the energy consumptions are comparable. This is because the write current of write-1 operation at 1.5 V SL voltage is comparable to that of write-0 operation at nominal voltage ( $BL = 0.9$  V).

**Effect of combination of voltage boosting and write pulse width duration**

Figure 22 illustrates the BER of write-1 operation under different voltage levels and write pulse width for access transistor size of  $W/L = 4$ . As expected, increasing the

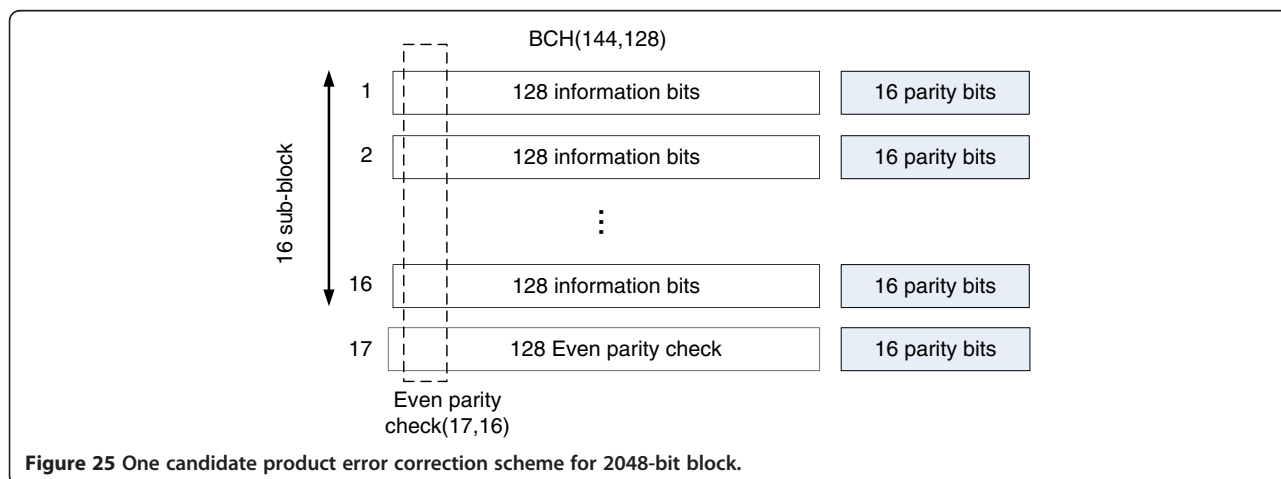


**Figure 25** One candidate product error correction scheme for 2048-bit block.

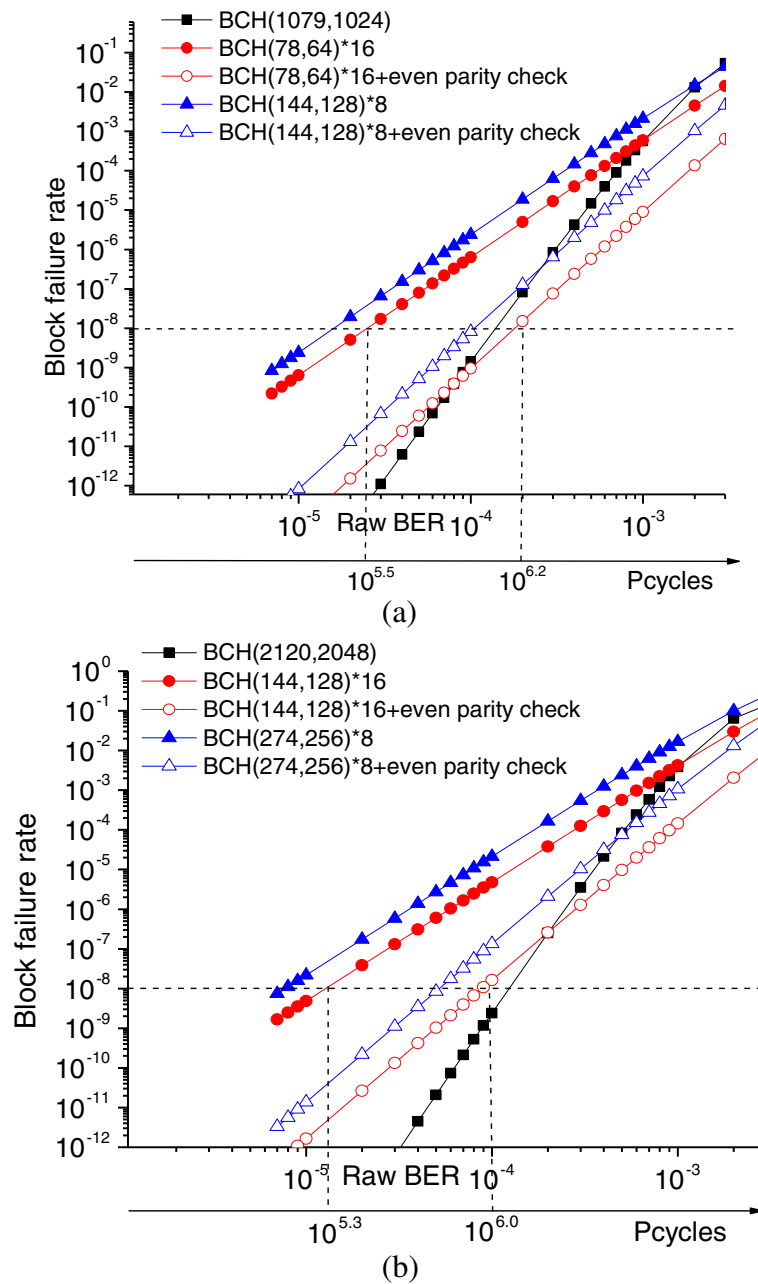


**Figure 26** Performance comparison between long BCH code and flexible ECC scheme for (a) 1024 bits and (b) 2048 bits.

pulse width reduces the BER for both write-0 and write-1 operations. Furthermore, boosting voltage level of SL during write-1 operation also reduces the write-failures. For

instance, when pulse width is 30 ns, write-1 BER =  $0.25 \times 10^{-2}$  when the boosted voltage is 1.1 V, whereas write-1 BER =  $0.4 \times 10^{-4}$  when the boosted voltage is 1.3 V.

**Table 6** Extra storage rates of different ECC schemes for three block sizes

	BCH(78,64)*8+ even parity check	BCH(78,64)*16+ even parity check	BCH(144,128)*8+ even parity check	BCH(144,128)*16+ even parity check	BCH(274,256)*8+ even parity check
512 bits	27%				
1024 bits		22.8%	21%		
2048 bits				16.4%	17%



**Table 7 Synthesis results of all candidate BCH codes**

	Encoder		Syndrome		KES		Chien search	
	Area ( $\mu\text{m}^2$ )	Power ( $\mu\text{w}$ )	Area ( $\mu\text{m}^2$ )	Power ( $\mu\text{w}$ )	Area ( $\mu\text{m}^2$ )	Power ( $\mu\text{w}$ )	Area ( $\mu\text{m}^2$ )	Power ( $\mu\text{w}$ )
BCH(144,128)	118	16	341	67	1404	248	188	300
BCH(542,512)	177	21	583	118	1836	478	244	444
BCH(1057,1024)	192	23	629	123	2145	533	286	489
BCH(2084,2048)	217	28	680	140	2618	669	328	578
BCH(552,512)	236	28	780	171	1978	512	392	699
BCH(1079,1024)	353	46	1133	233	3700	945	545	963
BCH(2120,2048)	430	56	1378	1354	4236	424	664	1203

Critical path is 0.59 ns for BCH(144,128), 0.65 ns for BCH(542,512), BCH(552,512), 0.74 ns for BCH(1057,1024), BCH(1079,1024), 0.89 ns for BCH(2084,2048), BCH(2120,2048).

In general, increasing these parameters reduces BER, but causes higher energy consumption per operation. For instance, let the average BER (read/write combined) after circuit-level techniques be set to  $10^{-5}$ . From read failure analysis, we see that  $W/L = 4$  achieves approximately  $\text{BER} = 10^{-5}$ . Even though, increasing  $W/L$  ratio improves the reliability for both read and write operations, it reduces the cell density and increases the energy consumption. Thus, it should be applied with caution and other options investigated.

Next, we investigate the combination of different write pulse widths and boosted SL voltages that can achieve the same target BER. For  $\text{BER} = 10^{-5}$ , we consider the following combinations of write pulse widths and boosted voltages: (60 ns, 0.9 V), (42 ns, 1.1 V), (31 ns, 1.3 V), and (25 ns, 1.5 V). Figure 23 illustrates the normalized average write power and energy consumption for all four cases. Since the average energy consumption of each write operation is comparable, higher voltage levels for write operation becomes more attractive due to its lower latency. However, increasing voltage also may create problems of MOSFET degradation due to hot carrier injection. Based on this analysis, we choose write pulse width of 31 ns and SL voltage of 1.3 V that achieves BER of approximately  $10^{-5}$ . While this is a significant reduction in the BER, for reliable memory operations, the target error rate is a lot lower. Such error rates are not achievable using only circuit-level techniques or using only ECC. In the following section, we describe our approach of applying ECC on top of circuit-level techniques to achieve high level of reliability with reduced cost.

### ECC schemes

#### ECC performance

One of the effective techniques to reduce the error rate in memories is through ECC. As described in “PRAM reliability” and “STT-RAM reliability” sections, raw error rate of MLC PRAM and STT-RAM can significantly be reduced using circuit-level techniques. For instance, the error rate of MLC PRAM can be reduced to  $10^{-4}$  by adjusting  $R_{\text{th}(10,00)}$  and the error rate of STT-RAM can be reduced to  $10^{-5}$  by voltage boosting and/or write pulse width adjustment.

In this section, we consider BFR as the performance metric since it represents the decoding performance more accurately compared to BER. The BFR for a constant block size  $N$  is calculated using a binomial distribution of uniform errors as:

$$\begin{aligned} \text{BFR} &= P(\text{error} > t) \\ &= \sum_{i=t+1}^N \binom{N}{i} \text{BER}^i (1 - \text{BER})^{N-i} \end{aligned} \quad (3)$$

where  $t$  is the correction strength of the ECC, and BER represents the raw error rate after applying circuit-level techniques.

In this article, the target BFR is set to  $10^{-8}$ . For STT-RAM, this target is constant during the whole lifetime. For PRAM, the error rate increases with number of programming cycles. Our goal is to maintain the same BFR throughout the devices’ lifetime.

To achieve the target BFR for both STT-RAM and PRAM, performances of ECC schemes with different error correction capabilities are shown in Figure 24. Three

**Table 8 Hardware overhead of ECC scheme for STT-RAM**

		Energy (pJ)	Latency (ns)	Area	Extra storage rate (%)
512 bits	BCH(542,512)	42.4	85.6	2840	5.5
1024 bits	BCH(1057,1024)	100.4	192.5	3525	3.1
2048 bits	BCH(2084,2048)	272.7	459.7	3838	1.7

**Table 9 Hardware overhead of ECC scheme for MLC-PRAM**

		Energy (pJ)	Latency (ns)	Area	Extra storage rate (%)
512 bits	BCH(552,512)	56.3	86.5	3386	7
1024 bits	BCH(1079,1024)	187.8	194.5	5732	5.9
2048 bits	BCH(2120,2048)	585.5	463.7	6717	1.7
	Flexible ECC	98.6	179.4	2051	16.4

block sizes namely 512, 1024, and 2048 bits are studied. The bottom three curves correspond to STT-RAM which can achieve raw BER of  $10^{-5}$  by circuit-level techniques. We see that  $t = 3$  codes are sufficient to achieve  $BFR \leq 10^{-8}$  for all three block sizes. The top curves correspond to MLC-PRAM which achieves  $10^{-4}$  by circuit-level techniques. We see that to meet  $BFR \leq 10^{-8}$ , stronger codes have to be adopted for large block size. For instance for block size 2K,  $t$  equals to 6. The advantage of circuit-level techniques is also demonstrated in Figure 24. For a 512-bit block size, when the raw BER can be reduced from  $10^{-3}$  to  $10^{-4}$ , it is sufficient to consider ECC with  $t = 4$  (instead of  $t = 8$ ). Using a weaker code results in significant reduction in the ECC overhead. The ECC schemes in Figure 24 are listed in Table 5.

The raw error rate of MLC PRAM increases as the number of programming errors increases. Thus, a flexible ECC scheme that can support higher error correction capability over time is desirable. Flexible ECC scheme is implemented by using product code which corrects errors in two dimensions. When the number of programming cycles is low, it is sufficient to do ECC in one dimension. As the number of programming cycles increases, the flexible ECC scheme uses ECC in two dimensions to enhance the error correction capability.

The structure of product code for a 2048-bit block is shown in Figure 25. The data are organized into 16 subblocks with BCH(144,128) operating on each subblock. During encoding, even parity check encoding is done along columns and BCH encoding is done along rows. The even parity encoder generates a 17th subblock on which BCH encoding is also done. During decoding, 17 BCH codes are decoded in the order from the 17th to the 1st followed by parity check. BCH(144,128) can correct two errors and detect more than two errors. After BCH decoding, the subblocks that contain more than two errors are marked and the position of the remaining errors in the marked subblock is detected by even parity check.

Performance comparison for 1K and 2K bit block sizes are shown in Figure 26. For 1K bit block size, both BCH(78,64)  $\times$  16 with even parity and BCH(144,128)  $\times$  8 with even parity meet the target BFR for raw BER of  $10^{-4}$ . BCH(78,64)  $\times$  16 with even parity is preferred because it has lower BFR as shown in Figure 26a. For 2K bit block size, before  $10^{5.3} = 2 \times 10^5$  programming cycles, regular BCH(144,128)  $\times$  16 is sufficient to ensure

that the BFR is lower than  $10^{-8}$ . After  $2 \times 10^5$  programming cycles, when the raw BER increases to  $10^{-4}$  even parity check is done in conjunction with BCH(144,128) to guarantee the same target BFR of  $10^{-8}$ .

Next, we present redundancy rate of the different ECC schemes. As shown in Table 6, the redundancy rate of product codes for 512-bit block and 1024-bit block is more than 20%. Thus, to keep the redundancy rate of memory below 20%, we only propose the flexible ECC scheme for 2048-bit block. Between two candidate flexible schemes for 2048 bits block, BCH(144,128)  $\times$  16 with even parity check is preferred because it has lower redundancy rate as shown in Table 6 and lower BFR as shown in Figure 26.

#### Hardware overhead

The BCH codes used for STT-RAM and PRAM have been synthesized in 45 nm technology using Nangate cell library [30] and Synopsys Design Compiler [31]. The synthesis results are listed in Table 7. BCH decoders use pipelined simplified inverse-free Berlekamp-Massey (SiBM) algorithm. The 2t-fold SiBM architecture [32] is used to minimize the circuit overhead of Key-equation solver while its latency is maximized. A P factor of 8 is used for all the syndrome calculation and Chien search circuitries. All the power numbers are simulated when the clock period is set to the critical path, which equals to the delay of 1 Galois field multiplier and 1 Galois field adder.

The energy, latency, area, and redundancy rate of the ECC schemes for STT-RAM are shown in Table 8. Since the error rate of STT-RAM does not change with data storage time or number of programming cycles, it only uses the ECC scheme BCH(2084,2048) on block size of 2048 bits to achieve  $BFR = 10^{-8}$ .

The comparison of energy, latency, area, and redundancy rate of the ECC schemes for MLC-PRAM are shown in Table 9. For 2K bits, to achieve BFR of  $10^{-8}$ , we could use BCH(2120,2048) or the flexible scheme which migrates from BCH(144,128) to BCH(144,128) with even parity when the raw BER increases from  $1.5 \times 10^{-5}$  to  $10^{-4}$  due to increased number of programming cycles. Although the redundancy rate of flexible scheme is significantly higher than BCH(2120,2048), it is still <20% and its ECC energy consumption is only 17% of BCH(2120,2048). Moreover, the latency of the flexible

ECC scheme is 38% of BCH(2120,2048) because it has shorter critical path and the BCH(144,128) units can be pipelined as in [32].

## Conclusion

In this article, we advocate the use of circuit parameter tuning and ECC to improve the reliability of emerging memory technologies such as MLC-PRAM and STT-RAM. We first analyze the error sources and build error models for these two technologies. Next we show that for MLC-PRAM, the hard and soft error rates can be reduced by optimal choice of threshold resistance. Similarly for STT-RAM, the hard error rate can be reduced by tuning the  $W/L$  ratios of the access transistors, boosting the voltage, and adjusting the write pulse width. These circuit-level techniques can help achieve BER of  $10^{-4}$  to  $10^{-5}$ . For higher reliability, ECC techniques have to be used in conjunction with the circuit techniques. We show that for STT-RAM, it is sufficient to use a BCH code with  $t = 3$  to achieve a BFR of  $10^{-8}$ . For MLC-PRAM, the raw BER increases with time and number of programming cycles and so a flexible ECC scheme that migrates to a stronger code is desirable. We propose one such product code scheme that uses BCH along rows and even parity along columns and achieves the desired BFR. We synthesize the ECC schemes in hardware and show that the hardware overhead, including additional storage, is quite low, making these schemes very attractive.

## Competing interests

The authors declare that they have no competing interests.

## Acknowledgment

This study was supported in part by a grant from NSF, CSR 0910699, and CNS 1218183. The authors would like to acknowledge the assistance from Zihan Xu and Ketul Sutaria on the memory modeling work.

Received: 16 April 2012 Accepted: 20 August 2012

Published: 3 October 2012

## References

1. BC Lee, E Ipek, O Mutlu, D Burger, Architecting phase change memory as a scalable DRAM alternative, in *International Symposium on Computer Architecture* (2009), pp. 1–12
2. X Wu, J Li, L Zhang, E Speight, R Rajamony, Y Xie, Hybrid cache architecture with disparate memory technologies, in *International Symposium on Computer Architecture* (Austin, Texas, USA, 2009), pp. 34–45
3. GW Burr, MJ Breitwisch, M Franceschini, D Garetto, K Gopalakrishnan, B Jackson, B Kurdi, C Lam, LA Lastras, A Padilla, B Rajendran, S Raoux, RS Shenoy, Phase change memory technology. *J Vac Sci Technol B* **28**(2), 223–262 (2010)
4. HS Philip Wong, S Raoux, S Kim, J Liang, JP Reifenberg, B Rajendran, M Asheghi, KE Goodson, Phase change memory. *Proc IEEE* **98**, 2201–2227 (2010)
5. T Kawahara, R Takemura, K Miura, J Hayakawa, S Ikeda, Y Lee, R Sasaki, Y Goto, K Ito, I Meguro, F Matsukura, H Takahashi, H Matsuoka, H Ohno, 2 Mb SPRAM (spin-transfer torque RAM) with bit-by-bit bi-directional current write and parallelizing-direction current read. *IEEE J Solid State Circuits* **43**(1), 109–120 (2008)
6. W Xu, H Sun, X Wang, Y Chen, T Zhang, Design of last level on-chip cache using spin transfer torque RAM. *IEEE Trans VLSI Syst* **19**(3), 483–493 (2011)
7. S Chatterjee, M Rasquinha, S Yalamanchili, S Mukhopadhyay, A scalable design methodology for energy minimization of STTRAM: a circuit and architecture perspective. *IEEE Trans VLSI Syst* **19**(5), 809–817 (2011)
8. XQ Wei, LP Shi, R Walia, TC Chong, R Zhao, XS Miao, BS Quek, HSPICE macro model of PCRAM for binary and multilevel storage. *IEEE Trans Electron Dev* **53**(1), 56–62 (2006)
9. N Papandreou, A Pantazi, A Sebastian, M Breitwisch, C Lam, H Pozidis, E Eleftheriou, Multilevel phase-change memory, in *17th IEEE International Conference on Electronics, Circuits, and Systems (ICECS)* (Athens, Greece, 2010), pp. 1017–1020
10. S Lavizzari, D Ielmini, D Sharma, AL Lacaite, Reliability impact of chalcogenide-structure relaxation in phase-change memory (PCM) cells—Part II: physics-based modeling. *IEEE Trans Electron Dev* **56**, 1078–1085 (2009)
11. W Xu, T Zhang, A time-aware fault tolerance scheme to improve reliability of multi-level phase-change memory in the presence of significant resistance drift. *IEEE Trans VLSI Syst* **19**(8), 1357–1367 (2011)
12. H Sun, C Liu, N Zheng, T Min, T Zhang, Design techniques to improve the device write margin for MRAM-based cache memory, in *ACM Great Lakes Symposium on VLSI* (Lausanne, Switzerland, 2011), pp. 97–102
13. Y Zhang, X Wang, Y Chen, STT-RAM cell design optimization for persistent and non-persistent error rate reduction: a statistical design view, in *IEEE/ACM International Conference on Computer Aided Design* (San Jose, CA, USA, 2011), pp. 471–477
14. J Lo, C Augustine, S Salahuddin, K Roy, Modeling of failure probability and statistical design of spin-transfer magnetic random access memory (STT MRAM) array for yield enhancement, in *IEEE Design Automation Conference* (Anaheim, CA, USA, 2008), pp. 278–283
15. A Nigam, CW Smullen, V Mohan, E Chen, S Gurumurthi, MR Stan, Delivering on the promise of universal memory for spin transfer torque RAM (STT-RAM), in *International Conference on Low Power Electronics and Design* (Fukuoka, Japan, 2011), pp. 121–126
16. C Yang, Y Emre, Y Cao, C Chakrabarti, Multi-tiered approach to improving the reliability of multi-level cell PRAM, in *IEEE Workshop on Signal Processing Systems* (Quebec, Canada, 2012)
17. Y Emre, C Yang, K Sutaria, Y Cao, C Chakrabarti, Enhancing the reliability of STT-RAM through circuit and system level techniques, in *IEEE Workshop on Signal Processing Systems* (Quebec, Canada, 2012)
18. Z Xu, K Sutaria, C Yang, C Chakrabarti, Y Cao, Hierarchical modeling of phase change memory for reliable design, in *IEEE International Conference on Computer Design* (Montreal, Canada, 2012)
19. F Bedeschi, R Fackenthal, C Resta, EM Donzè, M Jagasivamani, EC Buda, F Pellizzer, DW Chow, A Cabrini, G Calvi, R Faravelli, A Fantini, G Torelli, D Mills, R Gastaldi, G Casagrande, A bipolar-selected phase change memory featuring multi-level cell storage. *IEEE J Solid State Circuits* **44**(1), 217–227 (2009)
20. K Kim, SJ Ahn, Reliability investigation for manufacturable high density PRAM, in *IEEE 43rd Annual International Reliability Physics Symposium* (San Jose, CA, USA, 2005), pp. 157–162
21. S Lavizzari, D Ielmini, D Sharma, AL Lacaite, Reliability impact of chalcogenide-structure relaxation in phase-change memory (PCM) cells—Part I: experimental study. *IEEE Trans Electron Dev* **56**, 1070–1077 (2009)
22. D Elmhurst, M Goldman, A 1.8-V 128-Mb 125MHz multilevel cell Flash memory with flexible read while write. *IEEE J Solid State Circuits* **38**(11), 1929–1933 (2003)
23. N Papandreou, H Pozidis, T Mittelholzer, Drift-tolerant multilevel phase-change memory, in *IEEE International Memory Workshop (IMW)* (Dallas, TX, USA, 2011), pp. 1–4
24. S Kang, W Cho, B Cho, K Lee, C Lee, H Oh, B Choi, Q Wang, H Kim, M Park, Y Ro, S Kim, C Ha, K Kim, Y Kim, D Kim, C Kwak, H Byun, G Jeong, H Jeong, K Kim, Y Shin, A 0.1- $\mu\text{m}$  1.8-V 256-Mb phase-change random access memory (PRAM) with 66-MHz synchronous burst-read operation I. *IEEE J Solid State Circuits* **42**(1), 210–218 (2007)
25. J Kammerer, M Madec, L Hébrard, Compact modeling of a magnetic tunnel junction—Part I: dynamic magnetization model. *IEEE Trans Electron Dev* **56**, 1408–1415 (2010)

26. Y Chen, H Li, X Wang, W Zhu, T Zhang, A 130nm 1.2V/3.3V 16Kb spin-transfer torques random access memory with non-deterministic self-reference sensing scheme. *IEEE J Solid State Circuits* **47**(2), 560–573 (2012)
27. Y Ye, F Liu, S Nassif, Y Cao, Statistical modeling and simulation of threshold variation under dopant fluctuation and line edge roughness, in *45th Design Automation Conference*, 2008, pp. 900–905
28. Y Zhang, Y Li, A Jones, Y Chen, Asymmetry of MTJ switching and its implication to STT-RAM designs, in *Proceedings of the Design, Automation, and Test in Europe (Grenoble, France, 2012)*, pp. 1313–1331
29. Y Chen, X Wang, H Li, H Xi, Y Yan, Design margin exploration of spin-transfer torque RAM (STT-RAM) in scaled technologies. *IEEE Trans VLSI Syst* **18**(12), 1724–1733 (2010)
30. Nangate, Sunnyvale, California, Nangate, Sunnyvale, California (2008). *45nm open cell library*. <http://www.nangate.com>
31. Synopsys Design Compiler. <http://www.synopsys.com>
32. H Choi, W Liu, W Sung, VLSI implementation of BCH error correction for multilevel cell NAND flash memory. *IEEE Trans VLSI Syst* **18**(5), 843–847 (2010)

doi:10.1186/1687-6180-2012-211

**Cite this article as:** Yang et al.: Improving reliability of non-volatile memory technologies through circuit level techniques and error control coding. *EURASIP Journal on Advances in Signal Processing* 2012 **2012**:211.

**Submit your manuscript to a SpringerOpen<sup>®</sup> journal and benefit from:**

- Convenient online submission
- Rigorous peer review
- Immediate publication on acceptance
- Open access: articles freely available online
- High visibility within the field
- Retaining the copyright to your article

---

Submit your next manuscript at ► [springeropen.com](http://springeropen.com)

---